Micro-Explosion and Recycling of an Iron-Ethanol-Kerosene Slurry Fuel

ABOALHAMAYIE, Ahmed <http://orcid.org/0000-0002-3934-5976>, ZHANG, Yang, GHAMARI, Mohsen <http://orcid.org/0000-0002-4169-4729>, BANI ABDELRAHMAN, Ra'ed and ALSULAMI, Ibrahim K. <http://orcid.org/0009-0004-8222-1903>

Journal Pre-proof

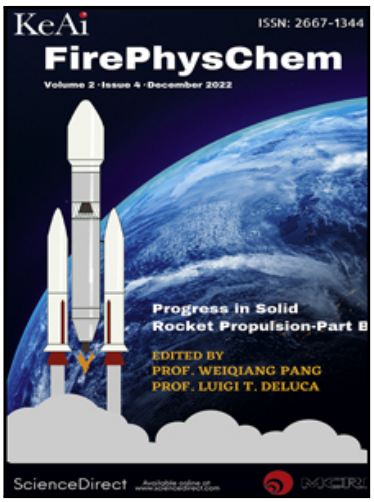

Micro-Explosion and Recycling of an Iron-Ethanol-Kerosene Slurry Fuel

Ahmed Aboalhamayie , Yang Zhang , Mohsen Ghamari , Ra'ed Bani Abdelrahman , Ibrahim K. Alsulami

PII: S2667-1344(26)00003-9
DOI: https://doi.org/10.1016/j.fpc.2026.01.003
Reference: FPC 264

To appear in: *FirePhysChem*

Received date: 18 September 2025
Revised date: 2 January 2026
Accepted date: 5 January 2026

Please cite this article as: Ahmed Aboalhamayie , Yang Zhang , Mohsen Ghamari , Ra'ed Bani Abdelrahman , Ibrahim K. Alsulami , Micro-Explosion and Recycling of an Iron-Ethanol-Kerosene Slurry Fuel, *FirePhysChem* (2026), doi: https://doi.org/10.1016/j.fpc.2026.01.003

Highlights:

- Kerosene coating delays Fe oxidation by up to ~95 °C.
- 5 wt% ethanol triples burn rate, halves combustion time.
- Micro-explosions peak at ~19,707 s^{-1} in 10 μm slurries.
- Closed loop: burn → H_2 reduce → FAST consolidate; >90% recovery.
- H_2-reduced FAST iron reaches ~165 HV with dense microstructure.

Micro-Explosion and Recycling of an Iron-Ethanol-Kerosene Slurry Fuel

Ahmed Aboalhamayie[a,1], Yang Zhang[a], Mohsen Ghamari[b], Ra'ed Bani Abdelrahman[c], Ibrahim K. Alsulami[d]

[a] *Department of Mechanical Engineering, The University of Sheffield, Sheffield S1 3JD, United Kingdom*

[b] *Department of Mechanical and Electrical Engineering, Wilkes University, Wilkes-Barre, PA 18766, USA*

[c] *School of Computing and Digital Technology, Sheffield Hallam University, Sheffield, S1 1WB, United Kingdom*

[d] *Department of Science, King Abdulaziz Military Academy (KAMA), Riyadh 13959, Saudi Arabia*

Abstract

Metallic iron is explored as a dual-purpose energy carrier and material feedstock by formulating a kerosene-based iron–ethanol slurry that serves both as a micro-explosive fuel where each droplet undergoes rapid internal bubble growth and fragments into many smaller droplets and as a source of recyclable iron. Single-droplet combustion experiments (with 30 wt% iron particles in kerosene + 5 wt% ethanol) demonstrate novel micro-explosion-driven combustion behavior. The addition of ethanol markedly enhances combustion, nearly quadrupling the burning rate and halving the burnout time

[1] *Corresponding Author*. The University of Sheffield, Department of Mechanical Engineering, Sir Frederick Mappin Building, Sheffield S1 3JD, United Kingdom. E-mail address: amaboalhamayie1@sheffield.ac.uk

compared to kerosene alone. Iron particle size is shown to govern the combustion mode: micron-scale iron produces intense, disruptive micro-explosions (with droplet fragmentation rates up to ~20,000 sec^{-1}) leading to complete burnout in as little as 0.3 s, whereas nano-iron yields more controlled burning (~1,700 sec^{-1}). Crucially, the hydrocarbon slurry provides an in-situ antioxidant effect, in the sense that the surrounding kerosene liquid acts as a protective barrier that separates the iron particles from oxygen, delaying iron oxidation during combustion and enabling non-oxidative storage of the metal fuel. Following combustion, over 90% of the iron oxide byproduct is recovered and regenerated into metallic iron via hydrogen reduction. The reduced iron is then compacted by Field-Assisted Sintering Technology (FAST), yielding dense iron compacts with fine microstructure and a Vickers hardness of ~165 HV approximately twice that of conventional pure iron (70–90 HV). This integrated combustion–reduction–sintering cycle highlights a circular iron loop in which the fuel itself becomes a high-value product. The findings showcase a sustainable, energy-efficient metal fuel platform that couples fire-driven micro-explosion phenomena with advanced materials processing, pointing to new opportunities in carbon-free combustion, functional material fabrication, and pyrotechnic applications.

Keywords: Droplet Combustion; Iron Particles; Combustion Time; Micro-explosion; Nonoxidative Storage; Hydrogen Reduction; Field Assisted Sintering Technology (FAST); Ethanol; Vickers microhardness

1. Introduction

The urgent shift from fossil fuels to renewable energy sources presents a critical challenge for advancing fuel and combustion technologies. Metallic fuels particularly iron and boron have recently emerged as promising candidates for carbon-free power generation [1–3], with micron-sized iron powder proposed as a renewable energy carrier [4,5]. Research into nano- and micron-scale iron particles (≤10 μm) aims to lower emissions and enhance energy efficiency at industrial scales [6,7]. For example, combustion of 38–53 μm iron under varying O_2 levels showed that, while peak temperature is relatively insensitive to particle size, burnout duration decreases markedly as oxygen concentration exceeds 50 % [8]. ReaxFF molecular dynamics studies by Sun et al. [9] indicate that, although up to 10 % defects elevate nanoparticle energy near melting, they do not alter melting points. Similarly, Wang Jin-yun et al. [10] demonstrated that nano-iron achieves a specific impulse of 3500 N·s/kg, underscoring its high energy density for transportation applications. Nanoscale iron has been applied in jet fuels to prevent coking: 7 nm particles, synthesized via sono-chemical methods and coated with oleic acid, bind chemically to organic components [11–12]. Below 110 °C, the coating protects the Fe^0 core from oxidation; above that temperature, coating decomposition allows oxygen to react with iron, forming FeOx catalysts that promote hydrocarbon oxidation and reduce ignition delays. Environmental factors strongly influence corrosion rates: microscale zero-valent iron (mZVI) corrodes slower than nanoscale iron in liquid but faster at low pH [13]; carbonyl iron corrosion degrades suspension stability and magnetorheological properties [14]; and carbon-encapsulated iron nanoparticles release iron under acidic conditions, compromising their structure and magnetic performance [15]. Because iron combustion proceeds via oxidation of metallic Fe to solid iron oxides, it is intrinsically

carbon-free at the point of use; consequently, replacing a fraction of the ethanol energy input with iron powder is expected to reduce the direct CO_2 emissions approximately in proportion to the displaced ethanol share. This expectation aligns with recent analyses of iron-based circular energy carriers and iron-fuel cycles, which demonstrate that iron powder acts as a CO_2-free fuel at the end-use stage and can markedly lower overall greenhouse-gas emissions when it substitutes carbonaceous fuels in power-generation pathways [77–79]. Indeed, iron nanoparticles exhibit rapid oxidation even at ambient conditions, generating distinct orange or brown oxides with minimal friction indicating a propensity for rapid corrosion. Incorporating iron particles (10 μm or 40 nm) at 30 % mass fraction into kerosene + 5 % ethanol (no surfactant) was hypothesized to mitigate premature oxidation and enhance combustion dynamics through intense micro-explosions. Ethanol's high volatility and oxygen content facilitate secondary atomization and droplet fragmentation both of which improve combustion heat transfer and reduce particulate emissions [16–22]. Single-droplet combustion serves as a model for spray processes in gas turbines, diesel engines, rockets, and industrial furnaces, where myriad interacting droplets determine overall performance [23]. Previous work by Li Qiao et al. [24] on 5 % mass-fraction iron nanoparticle suspensions and by Aboalhamayie et al. [25] on hybrid micron/nano iron colloids (which reduced total combustion time by 83 %) highlights the promise of dense iron slurries. Relative to earlier Fe, Al, and Mg metal-fuel work, which has mainly focused on metal–air/metal–water systems and nanofluid droplets in simple oxygenated carriers [24, 36, 1,], the present study is distinctive in two key aspects. First, highly loaded (30 wt%) Fe slurries in a kerosene carrier are employed; the kerosene acts simultaneously as the combustion medium and an in-situ antioxidant, raising the Fe oxidation onset temperature by ~95 °C for micron Fe and ~30 °C for nano Fe relative to uncoated powders. Second, the

introduction of a small ethanol fraction in 30 wt% Fe micron slurries (kerosene + 5 wt% ethanol) drastically alters droplet-scale combustion, with ethanol-driven micro-explosions nearly quadrupling the burning rate and reducing droplet burnout time by up to ~80% compared with neat kerosene, in contrast to prior ethanol nanofuels where such effects were not quantified for dense Fe slurries [61,62]. Following combustion, the resultant iron oxides are regenerated into metallic iron via hydrogen reduction ($Fe_2O_3 + 3H_2 \rightarrow 2Fe + 3H_2O$) a CO_2 free process widely studied for green steelmaking [26–27]. However, fine iron powders require consolidation to serve as reusable fuel or feedstock. Spark Plasma Sintering (SPS), also known as Field-Assisted Sintering Technology (FAST), applies pulsed DC current and uniaxial pressure to sinter powders rapidly at low temperatures, producing either high-porosity or fully dense iron structures [28]. An open question addressed in this work is whether hydrogen reduction followed by FAST consolidation can increase the microhardness of the as-reduced pellet. If confirmed, this would support the concept of iron as an energetic micro-explosive fuel for dual use as a recyclable fuel and as a better material in composite sintered products. In the iron fuel cycle, SPS/FAST closes the loop by converting reduced iron powder into solid pellets optimized for combustion kinetics enabling continuous reuse. Thermal behavior of uncoated and kerosene-coated iron powders was characterized via thermogravimetric analysis (TGA) and differential scanning calorimetry (DSC). High-speed imaging of single droplets quantified burning rates (K, mm^2/s), micro-explosion intensities (sec^{-1}), combustion durations (s), and peak internal temperatures (°C). Scanning Electron Microscopy (SEM), augmented by AI-assisted image processing, revealed residue morphologies and sub-droplet/jet formation. Combustion-derived iron oxides were collected and subjected to hydrogen reduction, with regenerated iron characterized by Energy-Dispersive X-ray Spectroscopy (EDS)

and elemental mapping. Finally, the reduced iron powders were consolidated using SPS/FAST to produce near-net-shape billet and its hardness evaluated by Vickers microhardness indentation testing was performed consolidated Fe (reduced iron powder). This integrated approach combustion, reduction, and consolidation demonstrates a sustainable, closed-loop cycle for iron as a carbon-free fuel, paving the way for next-generation, recyclable energy systems.

2. Materials and sample preparation technique

Two particle sizes of iron were investigated: Fe-40 nm (Nanostructured and Amorphous Materials Inc., Product ID 0262HW) and Fe-10 µm (Merck Life Science UK, Product ID 1038190500). Their microscopic morphologies and key physical properties are depicted in Fig. 1 and detailed in Table S1. kerosene, which is a pure kerosene derivative sourced from woody biomass, was developed at the Sustainable Aviation Fuels (SAF) Centre within the Energy 2050 Translational Centre at the University of Sheffield, and ethanol was purchased from Fisher Scientific.

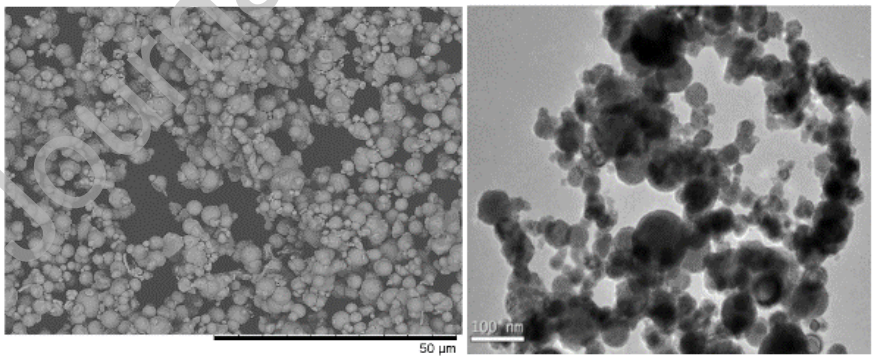

Fig. 1. SEM images of 10 µm iron particle (left) and 40 nm iron particles (right) [29]

Two fuel formulations were prepared: (1) kerosene containing 30% iron particles (micron- and nanoscale) without ethanol, and (2) kerosene with 5% ethanol containing 30% iron particles. Iron particles were weighed and manually mixed into the base fuel

(kerosene), and the mixture was sonicated in an ultrasonic ice bath (Elmasonic S10H). The slurry suspension was maintained in an ice bath during sonication, and its mass was measured before and after loading to verify that no evaporation or mass change occurred. This precaution was taken because kerosene has a higher evaporation rate than, for example, diesel fuel, and the ethanol added to the slurry also evaporates rapidly. Each sample volume was 20 mL, and the sonicator power was set to 30%. To optimize micro- and nanofuel preparation, various sonication times were tested; intermittent sonication for 45 minutes provided the most effective particle dispersion. For the kerosene + 5% ethanol formulation, kerosene and ethanol were first mixed on a magnetic stirrer for 20 minutes to ensure miscibility and homogeneity. Iron particles of both sizes were then added to reach 30%, and the mixture underwent ice-bath sonication for 45 minutes. Stability tests were evaluated using two tactics: (1) physical observation by emitting a flash of light to check stability, and (2) the advanced method shown in the schematic of the experimental apparatus in Fig. 2. The experimental apparatus in Fig. 2, meticulously designed in the lab, consists of an infrared (IR) laser, an IR receiver (detector), Arduino Mega 2560 microcontroller, micro sliders, linear actuators, a robotic arm gripper, a thermocouple amplifier, a Type-K thermocouple, and a sample holder. This setup was designed to detect any temperature rise above ambient conditions, mitigate potential measurement uncertainty caused by radiation effects from suspended particles, and precisely determine the settling rate, which is 5 minutes for the micron slurry (30% Fe-10 μm + kerosene), the nano slurry (30% Fe-40 nm + kerosene), the 30% Fe-10 μm + kerosene + 5% ethanol slurry, and the 30% Fe-40 nm + kerosene + 5% ethanol slurry, since the particle densities are the same and higher than that of the base fuel. It is worth mentioning that the kerosene + 5% ethanol formulation was placed in the apparatus to detect any reflection of the laser beam or any phase

separation; however, the multicomponent fuel remained homogeneous for days without separation due to the low to negligible water content of the ethanol and the good storage conditions for the fuel before the addition of iron particles. The fuel was freshly prepared before each experiment day. This finding was used to control the droplet-deployment suspension combustion experiment so that it did not exceed 2 minutes, ensuring accuracy. The Type-K thermocouple operates within a temperature range of −200 °C to +1350 °C, with an output resolution of 0.25 °C. However, Type-K thermocouples typically exhibit an accuracy of approximately ±4 °C. Reproducible code and workflow are documented in Supplementary Appendix A. Visual inspection showed that suspensions of Fe-40 nm and Fe-10 μm in kerosene and in kerosene + 5% ethanol remained stable for 5 minutes post-sonication. Accordingly, samples were kept in the sonication bath until just before each experiment. The microsyringe was loaded with the slurry in under 25 s, and deposition onto the SiC fiber required 15 s. Because the system was fixed in place and synchronized, the command introduced only a 1 s delay, after which ignition occurred. The total combustion time did not exceed 1.5 s for the nanoscale case and 0.5 s for the microscale case, placing the overall duration of each experiment in the ~5 min range. The 5-min window was maintained. While laboratory stability tests showed macroscopic homogeneity for approximately 5 minutes post-sonication, it is important to note that these quiescent conditions do not fully reflect dynamic combustion systems. In practical applications, fuel is continuously pumped and atomized, which actively prevents settling. Furthermore, as demonstrated in subsequent sections, the addition of ethanol promotes vapor-driven micro-explosions, enhancing secondary atomization and iron dispersion. Evaporation-induced Stefan flow also drives internal circulation, further counteracting particle settling. Given that each droplet combusts in less than 1 second, significantly faster than any

notable sedimentation, the measured laboratory stability is deemed sufficient for both experimental control and practical use.

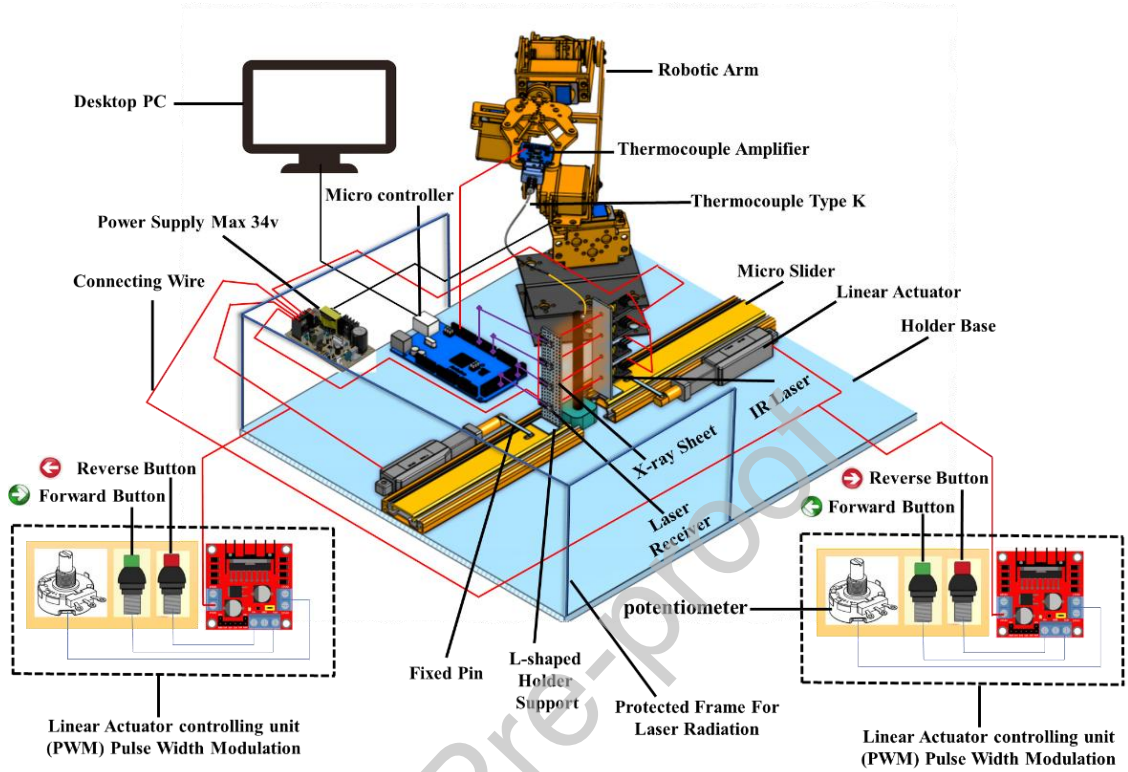

Fig. 2. Differential sedimentation rate apparatus

3. Experimental methodology

Fe–40 nm and Fe–10 μm iron particles both uncoated and coated with kerosene were characterized to elucidate their settling, thermal, combustion, and post-combustion consolidation behaviors. For thermal analysis, iron particles were dispersed in kerosene and sonicated for 45 minutes; a diametrically magnetized N52 Neodymium rod magnet (5 mm × 50 mm) then isolated the coated particles, which were sealed for testing. Thermogravimetric analysis (TGA) and differential scanning calorimetry (DSC) (TA Instruments Q600) were conducted in flowing air (100 mL min^{-1}) using open alumina pans, with a 1 min isothermal hold followed by a 5 °C min^{-1} ramp from 25 to 1400 °C to emulate oxidizing droplet combustion and thermite conditions; the Q600 employs a

dual-beam balance (0.1 μg resolution) and Pt/Pt–Rh thermocouples (rated to 1500 °C), and calibration included an empty-pan baseline plus standard heat-flow and mass calibrations before measurement.

Droplet combustion experiments utilized a custom setup integrating precision positioning, ignition control, and high-speed imaging as illustrated in Fig. 3(a). A 100 μm SiC fiber was mounted on a linear actuator to support a fuel droplet dispensed by micro-syringe. A second linear actuator carried a robotic-arm gripper equipped with a Kanthal A-1 wire (40 mm length, 0.127 mm diameter) that served as the ignition element. This wire, held between ceramic insulators and connected to a terminal block, the heating element was replaced after each experiment. Uncertainty propagation for the hot-wire energy measurement is detailed in Supplementary material file Appendix B.

It was driven by an electronic circuit that simultaneously triggered the Photron SA4 high-speed camera (2000 fps) and applied current represented in Fig. 3(d). After a 300 ms heating interval, the gripper retracted the wire to –45°, terminating ignition and recording; the system then reset for subsequent runs as shown in Fig. 3(c). To measure internal droplet temperature, the SiC fiber was replaced with a bare-junction Type-K thermocouple (Ø 0.10 mm, length ~300 mm; Omega Engineering, e.g., CHAL-005-BW), as shown in Fig. 3(b); the droplet was deposited directly on the junction, and both wire ends were clamped to prevent movement during heating or micro-explosions. The thermocouple signal was conditioned by an in-head 4–20 mA transmitter (RS PRO TX203TC, RS 381-7132; Type-K accuracy ±0.1% FS ±0.5 °C, CJC ±0.5 °C) and digitized with a National Instruments USB-6210 at 1000 Hz for real-time logging. To minimize drift and oxidation errors, a fresh thermocouple was installed after every experiment: for the slurry iron ethanol tests (three fuels), each fuel was conducted five

times with a new thermocouple for each replicate; for the thermite tests (three formulations), each formulation was likewise run five times, replacing the thermocouple for every replicate. Synchronization among the heating element, servomotor, and imaging system was achieved using an Arduino Mega 2560 microcontroller. Implementation details and source code are included in Supplementary material file Appendix C. Combustion imagery was backlit and diffused; recorded frames were processed in NASA Spotlight [30–32] to remove fiber shadows. Advanced image-processing routines quantified sub-droplets and oxide-particle jets: each frame was converted to grayscale, denoised with a Gaussian blur [33], sharpened to accentuate edges, and binarized via adaptive thresholding [34]. Morphological closing/opening refined particle boundaries, and connected-component analysis [35] labeled individual features. Pixel length calibration was performed with a reference target of known dimensions. Frames were preprocessed (temporal smoothing/denoising and contrast normalization), then binarized using an adaptive threshold. Standard morphological operations (erosion–dilation and opening–closing) were applied to suppress speckle and refine the droplet boundary, after which the contour was extracted to track equivalent-diameter and surface deformation versus time. Full calibration procedures, image-processing workflows are provided in Supplementary Appendix D.

Post-combustion residues and evaporation agglomerates were collected directly from the fiber and examined under a Hitachi TM3030 tabletop SEM. To isolate non-combustion agglomerates, the heating element was positioned farther from the droplet and the temperature raised until only base fuel evaporation occurred; the resulting deposits on the fiber were then analyzed. This comparison between combustion ashes and evaporation agglomerates illuminated differences in particle morphology under oxidative (combustion) versus purely evaporative conditions.

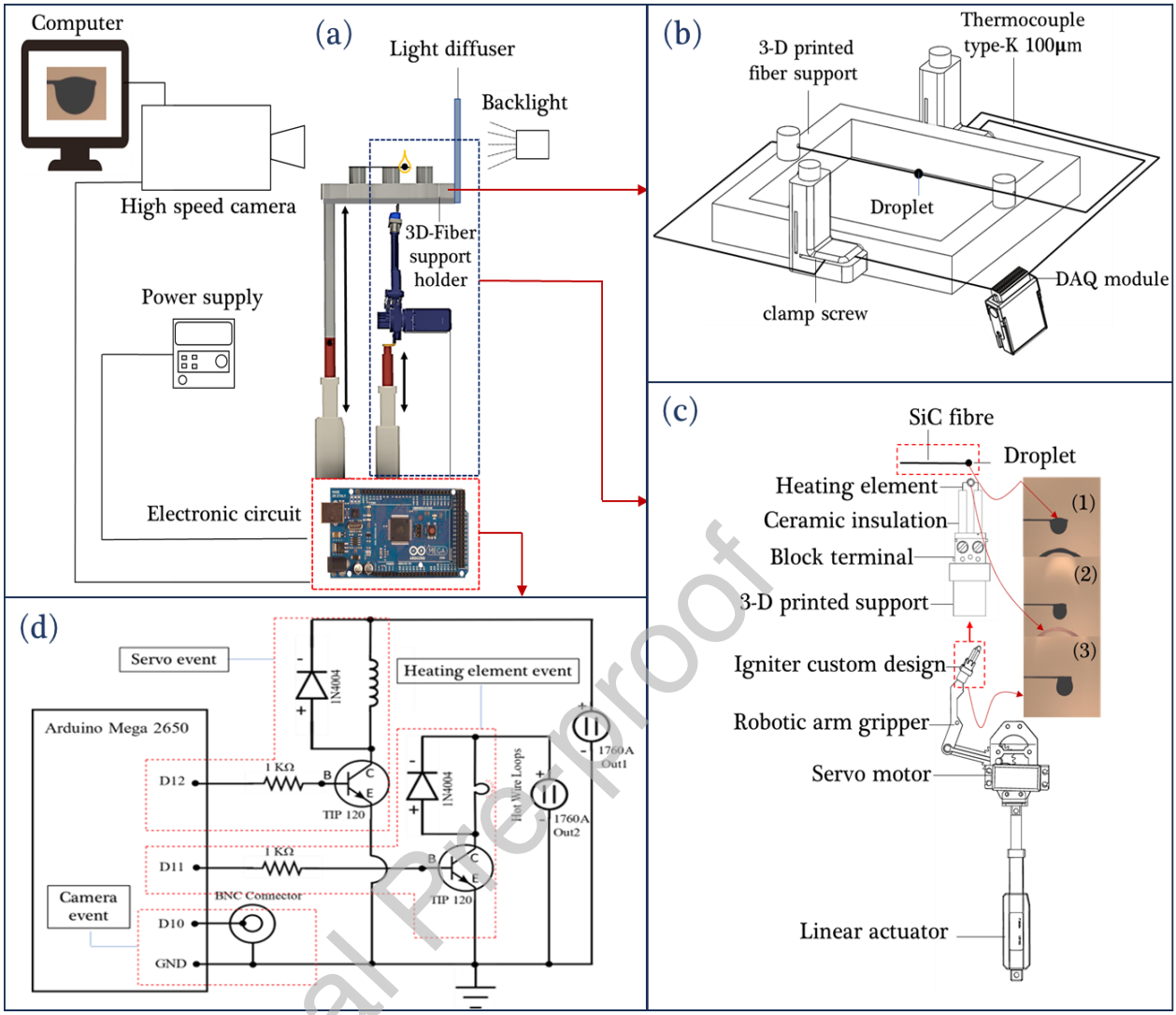

Fig. 3. (a) Droplet combustion setup; (b) internal temperature measurement using a 100-µm K-type thermocouple; (c) ignition system; (d) electronic synchronization circuit.

Iron oxide residues collected from combustion experiments were first tested magnetically to identify magnetite-rich fractions. Samples were loaded into a glass reaction tube, purged with hydrogen (H_2) at 0.1 L/min for 2 minutes to remove residual oxygen, then reduced continuously at 800–900 °C under the same H_2 flow for 35 minutes per batch as captured in Fig. 4. After each reduction cycle, magnetic separation isolated metallic iron particles. Five identical runs (5 g per run) yielded 20 g of reduced

material. Scanning Electron Microscopy (SEM) and elemental mapping were used to confirm phase conversion and evaluate the morphology after reduction. The analysis was performed using an Inspect F50 field-emission SEM, equipped with an Oxford Instruments energy-dispersive X-ray spectroscopy (EDS) system for compositional characterization.

Consolidation of reduced iron was performed using an FCT HP D 25 Field-Assisted Sintering/Spark Plasma Sintering Furnace under vacuum (~100 Pa) with a constant uniaxial load of 3 kN as in the schematic in Fig. 4. Sample was heated to 800 °C and held for 15 minutes to promote neck growth and densification; dual pyrometers and embedded thermocouples ensured thermal uniformity. All process parameters, including force, temperature, pressure, and electrical input, were continuously recorded. Following sintering, cylindrical specimens were sectioned using a Secotom-50 precision saw (200 rpm blade speed, 0.05 mm/s feed), then mounted in conductive bakelite at 180 °C under 290 bars. Mounted samples were ground and polished automatically on an Automet 250 using 9 µm and then 3 µm diamond suspensions. Pre-etch inspections with a Nikon Eclipse LV150 optical microscope and a Hitachi TM3000 SEM evaluated pore distribution. Specimens were chemically etched in nitric acid for 30 seconds, rinsed with isopropanol, and dried to reveal grain boundaries and pore networks under subsequent SEM/optical imaging. Finally, the elemental composition of the sintered iron was quantified using a FISCHERSCOPE X-RAY XAN 250 EDXRF spectrometer, verifying the efficacy of hydrogen reduction and vacuum FAST consolidation. Finally, Vickers microhardness testing was performed on consolidated powder-metallurgy specimens Fe (reduced iron powder using a MITUTOYO Vickers Microhardness Tester with a 136° diamond indenter at 1 kgf (HV1) and 15 s dwell. Five indents were made on the sample at different, representative locations with proper

spacing from edges/pores. The two diagonals of each impression were read manually through the microscope, and hardness values were obtained from the Vickers Hardness Number table (Model HM-101, OBJ. lens 50×) corresponding to the measured diagonal lengths; results are reported in standard notation as HV 1/15.

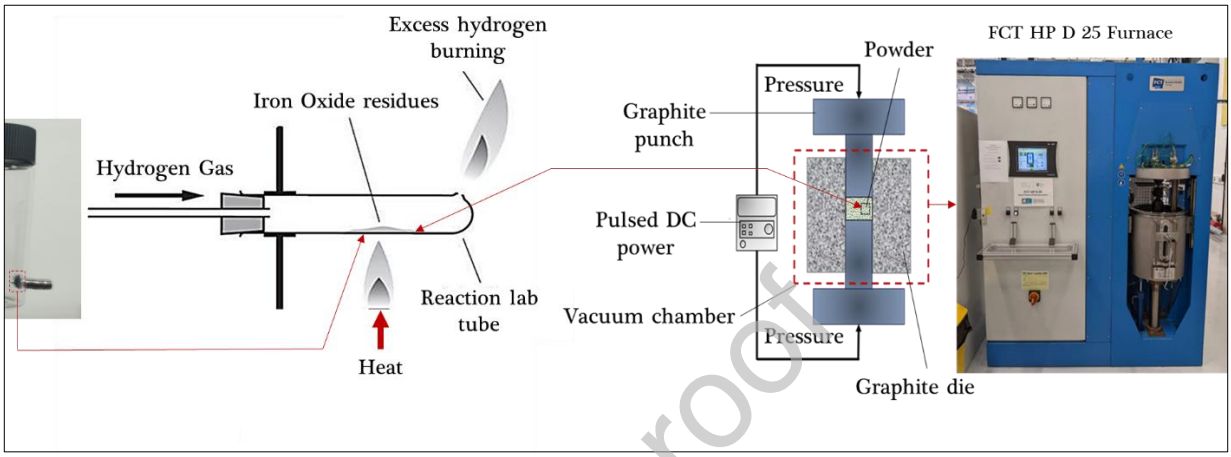

Fig. 4. Iron oxide reduction and sintering process

This experimental workflow therefore links single-droplet combustion, residue collection, hydrogen reduction and FAST consolidation into a single closed-loop process. In the following Results section, the combustion and micro-explosion characteristics of the different fuel formulations are first analyzed (Sections 4.1–4.4), and the behavior of the resulting combustion-derived iron-oxide powders during hydrogen reduction and FAST consolidation is then examined (Section 4.5).

4. Results

4.1. Thermal oxidization of pure powders of Fe particles and coated Fe powders

Uncoated Fe-10 µm in Fig. 5(a) began gaining mass at 237 °C, peaking at 42.2 % increase at 873 °C consistent with Fe → FeO → Fe_3O_4 → Fe_2O_3 (theoretical 43 % for 2 Fe → Fe_2O_3) [36] and exhibited a 26 mW exotherm at 500.7 °C marking oxidation onset; above 850 °C, mass fell by 3–5 % (850–1400 °C) as Fe_2O_3 partially reduced to

Fe_3O_4/FeO [37]. Combustion residue EDS in Fig. 6 of Fe-10 μm in kerosene + 5 % ethanol revealed regions with 92.2–94.7 wt % Fe (5.2–6.2 wt % O) (Spectra 11, 13, 17, 20, 21), indicating metallic cores, whereas Spectra 12, 15, 16, 18 (77.9–84.3 wt % Fe, 12.0–21.0 wt % O) correspond to partial Fe_3O_4/Fe_2O_3; Spectrum 19 (50.4 wt % Fe, 37.4 wt % O, 11.8 wt % C) reflects heavily oxidized, carbon-rich zones, supporting a core shell oxidation mechanism after micro-explosions. Kerosene-coated Fe-10 μm in Fig. 5(b) lost ~41 % mass at 175.3 °C due to kerosene evaporation (DSC endotherm 167.6 °C/exotherm 287.4 °C, 166–190 °C), then oxidation began at 332.3 °C: by 577 °C mass rose from 60 % to 76 % (+16 %) with a 5.86 mW exotherm at 483 °C; from 577 °C to 1219 °C mass increased from 76 % to 84 %, and from 1219 °C to 1394 °C mass declined from 84 % to 80 % (−4 %), confirming Fe → Fe_2O_3 conversion (~40 % net gain, close to theoretical 43 %). Uncoated Fe-40 nm in Fig. 5(c) began mass gain at 171.2 °C, with an exotherm of −1.4 mW at 236.6 °C; oxidation peaked at 1113.9 °C, followed by an endotherm at 1348.3 °C, indicating complete Fe_2O_3 formation. Kerosene-coated Fe-40 nm Fig. 5(d) lost volatile kerosene to 177.1 °C, then oxidized from 201.1 °C (2.88 mV peak at 237.2 °C) through a second exotherm at 396.1 °C; at 1102.9 °C mass rose from 78 % to 105.9 % (+35.7 %, ~7 % below theoretical 43 %), completing oxidation by 1388.4 °C with a 1400 °C endotherm confirming Fe_2O_3. Tables 1–2 summarize these TGA-DSC results, showing that kerosene coating raises oxidation onset by ~95 °C (micron) and ~30 °C (nano), with coated Fe-10 μm requiring 332–600 °C versus 237–850 °C uncoated, and coated Fe-40 nm needing 201–1348 °C versus 171–1113 °C uncoated. Moreover, DSC in Table 1 measurements represent the micron-scale Fe powder (10 μm) exhibits a total exothermic heat release Q of ~45.8 J (37.4 J in the coated form), whereas the 40 nm Fe powder releases only ~0.22–0.27 J. This more than two-order-of-magnitude difference in energy output. In analysis TGA T_e, endset

temperature (˚C); is defined as the temperature where the mass reaches its final plateau, whereas DSC Te corresponds to the endset of the main exothermic oxidation peak. In nano-Fe, most of the oxidation enthalpy is released below ~260 °C (DSC), but slow diffusion-limited oxidation and phase evolution continue to higher temperatures, so the mass gain in TGA stabilizes only close to 1100°C. Thus, coated micron particles offer superior long-term oxidation resistance, whereas nanosized powders oxidize more readily representing in Fig. S1. Whether droplet combustion achieves these internal temperatures and whether particle morphology facilitates heat diffusion to trigger oxidation will be examined in subsequent sections.

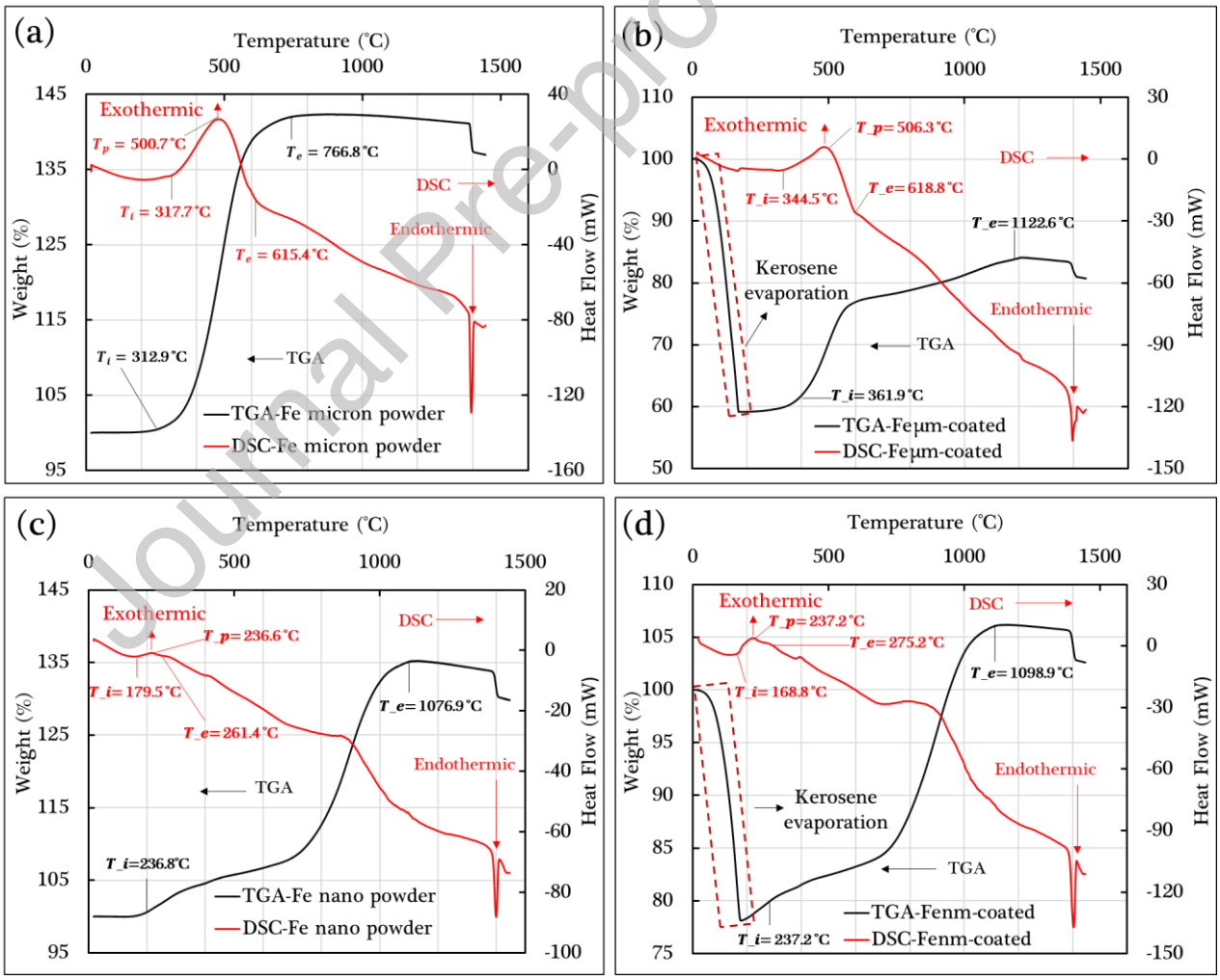

Fig. 5. (a, c): TGA-DSC of iron micron and nano size particles in powder form, and (b, d) coated with kerosene

Table 1. The DSC results of samples

Samples	T_i	T_p	T_e	Q
Fe-10 µm powder form	317.7	500.7	615.4	45.83
Fe-40 nm powder form	179.5	236.6	261.4	0.22
Fe-10 µm coated form	344.5	506.3	618.8	37.4
Fe-40 nm coated form	168.8	237.2	275.2	0.27

Note: T_i, onset temperature (˚C); T_e, endset temperature (˚C); T_p, peak temperature (˚C); Q heat release in J.

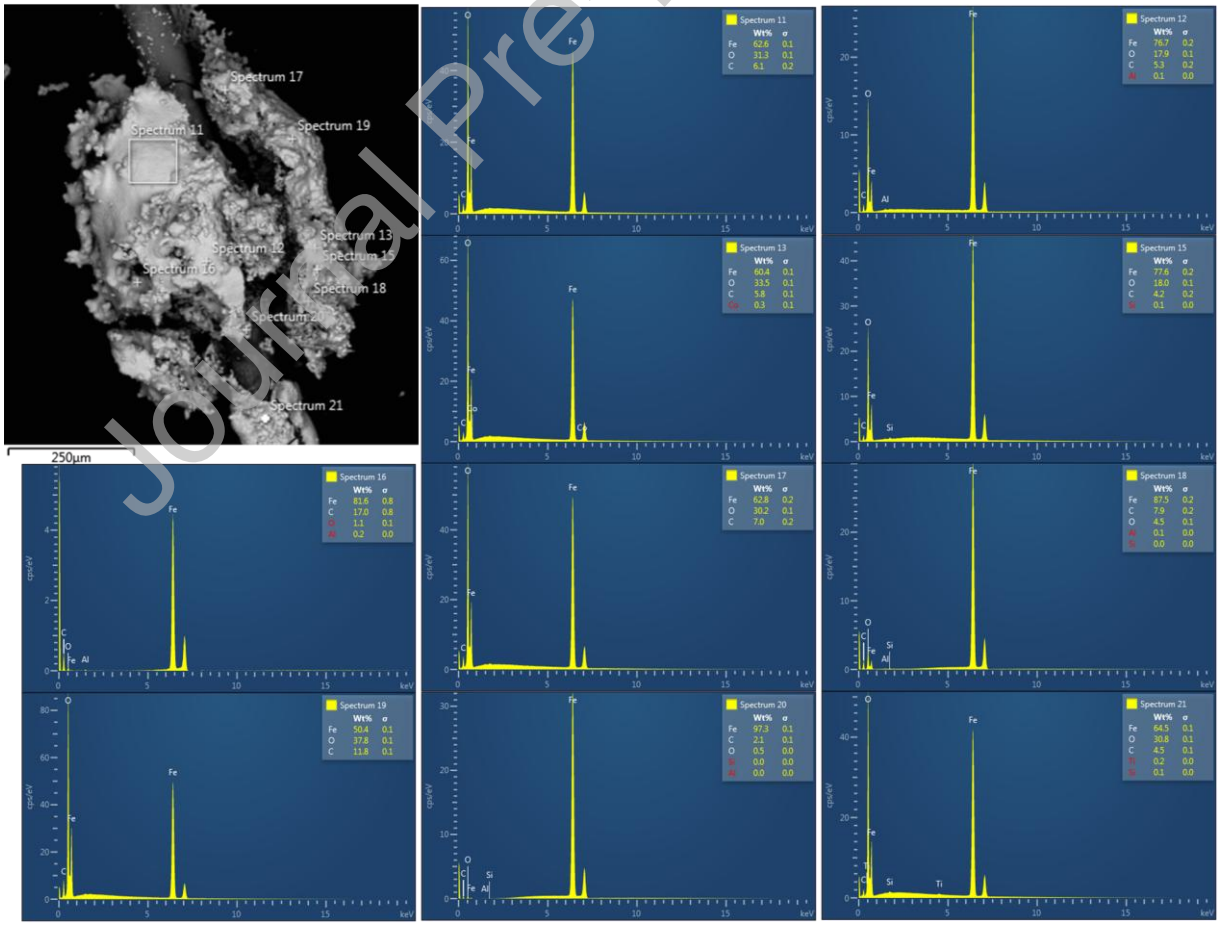

Fig. 6. Residues of Fe-10 μm in kerosene and ethanol were collected and analyzed using Energy-Dispersive X-ray Spectroscopy (EDS)

Table 2. The TGA results of samples

Samples	T_i	T_e	MC
Fe-10 μm powder form	312.9	766.8	42.2
Fe-40 nm powder form	236.8	1076.9	35
Fe-10 μm coated form	361.9	1122.6	40
Fe-40 nm coated form	237.2	1098.9	35.7

Note: T_i, onset temperature (˚C); T_e, endset temperature (˚C); MC, mass change (%).

4.2. Droplet combustion

The burning rate of a droplet can be evaluated using the classical d^2-law of droplet combustion as expressed by Equation (1). Here, d, d_0, t, and k are instantaneous and initial droplet diameters, time, and droplet combustion rate, respectively. In order to determine the burning rate from the experimental data, the time variation of the squared diameter during combustion was plotted against time, as shown in Fig. 7 and the slope of the resulting diagram was considered as the burning rate.

$$\left(\frac{d}{d_0}\right)^2 = 1 - k\left(\frac{t}{d_0^2}\right) \qquad (1)$$

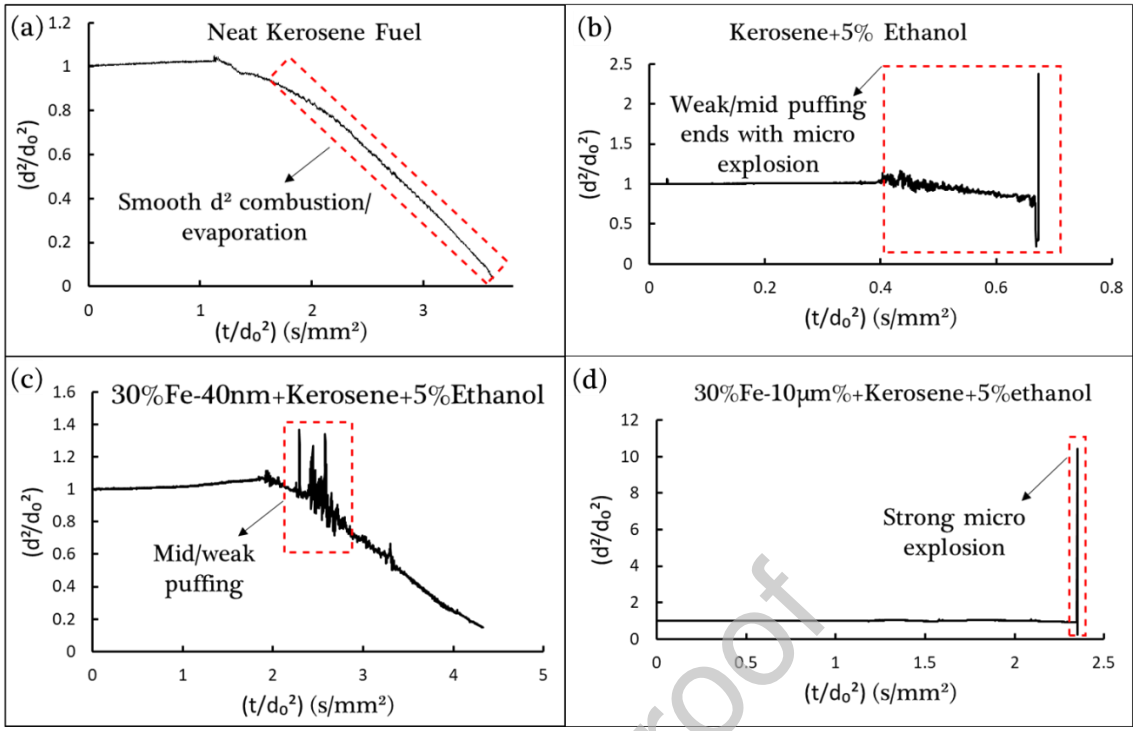

Fig. 7. Evolution of normalized droplet diameter square for (a) neat kerosene; (b) kerosene + 5% ethanol; (c) 30% Fe-40 nm particles + kerosene + 5% ethanol; (d) 30% Fe-10 μm + kerosene + 5% ethanol.

Fig. S2 presents the combustion stages of 30 % Fe-40 nm in kerosene. In Zone (a), the droplet remains stable at its initial diameter. Zone (b) marks rapid expansion and ignition, after which Zone (c) follows the classical d^2-law linear (d^2/d_o^2) vs. (t/d_o^2). In Zone (d), four sub-stages occur: (1) rapid vaporization releasing clustered droplets into the flame; (2) weak puffing/micro-explosions producing transient distortions; (3) formation of spherical iron clusters that intensify the flame; and (4) flame extinction and complete combustion of agglomerated iron. Five replicates confirmed repeatability and coherence. SEM analysis of post-combustion residues in Fig. S3(a) and Fig. S3(b) reveals dark orange-brown clusters perforated with crater-like holes, evidence of late-stage micro-explosions mechanism in Fig. S5 (parts 1 and 2). These agglomerates exhibit minimal mass loss, yielding only slight increases in burning rate (k) and total combustion

time (Section 4.3). Fig. S4 depicts 30 % Fe-10 µm in kerosene, where gravitational and surface-tension forces drive complex droplet rearrangements on the SiC fiber. Micron particles' lower surface area impedes adhesion in low-viscosity kerosene. Combustion phases include droplet expansion and ignition, centralization of particles causing further expansion, evaporation-induced agglomeration that restores sphericity, and strong edge puffing with oxidized sparks. Maximum agglomeration produces a fully spherical iron cluster before droplet detachment (~0.6 s after flame appearance), precluding complete capture by high-speed imaging. The schematic in Fig. S5(a) and Fig. S5(c) outlines this mechanism. These observations motivate Section 4.2.3's discussion on formulating a fully oxidizing slurry to mitigate large agglomerate formation and optimize combustion performance.

4.2.1. Combustion of kerosene and 5% ethanol

The decay pattern of droplet diameter conforms to the d^2-law, indicating that kerosene droplet combustion is consistently governed by evaporation, as shown in Fig. 7(a), irrespective of the addition of Fe-nm particles or Fe-µm particles as previously shown in Fig. S2 and Fig. S4. To enhance the ignition and combustion performance of Fe-nm or Fe-µm in kerosene nano-micron fluid/slurry fuel droplets, the evaporation process of the kerosene droplet must be controlled through the incorporation of ethanol. The combustion process of the kerosene + 5 % ethanol mixture initiates with expansion, followed by ignition, as illustrated in Fig. 7(b). The appearance of the flame is enveloped and exhibits lower radiation intensity, attributed to the introduction of ethanol. The droplet undergoes internal nucleation, leading to the formation of small bubbles due to the differing boiling points between kerosene and ethanol. Concurrently, the droplet experiences significant distortion as these small spherical bubbles forms and circulate inside the droplet with limited growth from t = 0.36 s to t = 0.49 s, as shown

in Fig. 8. When the internal bubble is trapped at the edge of the surface, a micro-explosion results in substantial fragmentation of the droplet into sub-droplets at t = 0.718 s. Fig. 7(b). illustrates the d^2-law of combustion during the (t/d_0^2) period from 0.4 to 0.6, where the strong distortion of the droplet culminates in a peak at (d^2/d_0^2) = 2.38, driven by a pronounced micro-explosion. The faster combustion rate of kerosene-ethanol blend is attributable to the solvent's high extraction power, as explained in section 4.3.

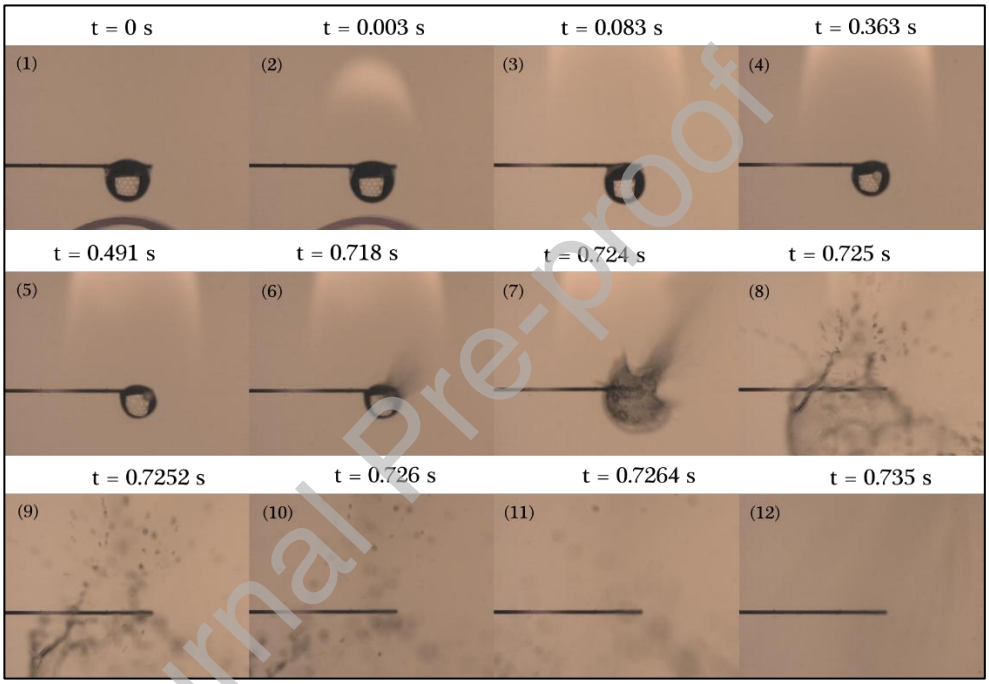

Fig. 8. Droplet combustion of kerosene with 5% addition of ethanol and time (in seconds, s)

When ethanol is introduced to kerosene, ethanol molecules can interact with the hydrocarbon chains of kerosene through van der Waals forces. However, because kerosene molecules do not engage in hydrogen bonding, ethanol does not disrupt hydrogen bonds within kerosene. Instead, ethanol may act as a cosolvent, slightly enhancing the solubility of certain substances in kerosene by interacting with both polar and nonpolar components; thus, the larger the surface area available for combustion, the higher the

combustion rate. The higher maximum pressure in the ethanol sample may be attributed to the higher volatility of ethanol compared to kerosene, as the vapor pressure of ethanol is more than 15 times that of kerosene at room temperature [38]. It is noteworthy that beyond a concentration of 5%, droplets undergo a strong micro-explosion as heating begins. From this perspective, ethanol modifies the overall combustion characteristics of kerosene, enabling it to function as a multi-component fuel with shorter combustion times, higher burning rates, and improved efficiency in micro-explosion and sub-droplet fragmentation.

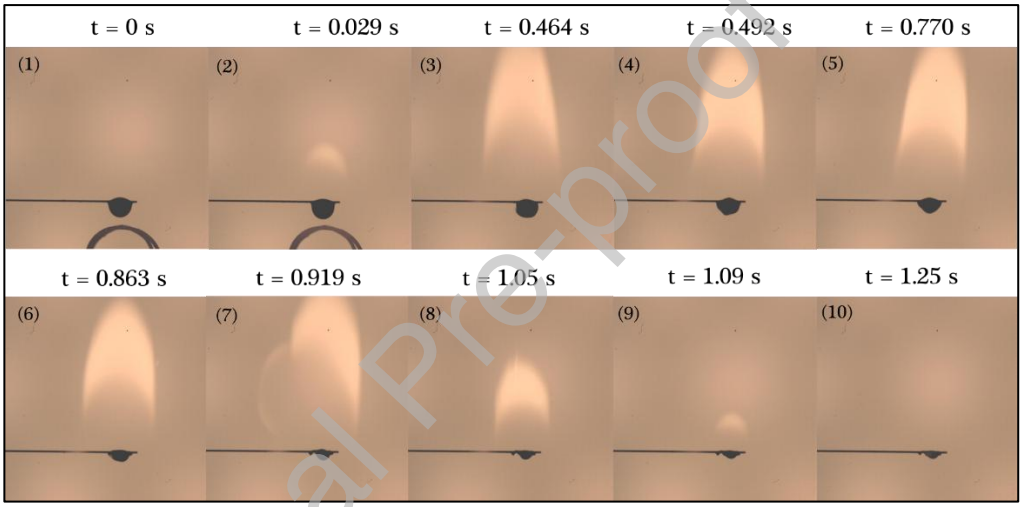

Fig. 9. Sequence of images with respect to time (in seconds, s) shows combustion of 30% Fe-40 nm + kerosene + 5 %ethanol

4.2.2. Combustion of (30% Fe-40 nm + kerosene + 5% ethanol)

Fig. 9 shows the combustion sequence of a (30% Fe-40 nm + kerosene + 5% ethanol) droplet, highlighting significant droplet distortion throughout the combustion process. This distortion led to the rapid ejection of attached nanoparticles into the flame zone, where oxidation occurred due to the higher oxygen concentration. The addition of ethanol reduced nanoparticle agglomeration, decreased total combustion time, and increased micro-explosion intensity as defined by Equation 2. Ethanol's lower boiling point and higher volatility compared to kerosene facilitated immediate nucleation,

strong puffing, and significant mass loss. The presence of ethanol resulted in a more pronounced ejection of small jets. As shown in Fig. 7(c), the normalized combustion time increased from $(t/d_0^2) = 2.295$ to $(t/d_0^2) = 2.713$, with 15 peaks of micro-explosion as shown in Fig. S6 and further detailed in section Following these events, the droplet evaporated according to the d^2-law from $(t/d_0^2) = 2.85$ to $(t/d_0^2) = 4.32$, leaving minimal residue on the SiC fiber with the microscopic structure as further discussed in section 4.3.

4.2.3. Combustion of (30% Fe-10 µm + kerosene + 5% ethanol)

The incorporation of ethanol amplifies the phenomena of puffing and abrupt explosions, resulting in a reduced total combustion time and enhanced particle oxidation. Ethanol effectively swells the iron particles, generating weak gel structures that inhibit sedimentation in droplets of dense concentration, thereby maintaining suspension on the SiC fiber. The increased internal vapor pressure, resulting from the differential boiling points of kerosene and ethanol, facilitates rapid and intense micro-explosions, preventing droplet agglomeration and enhancing surface tension between the droplet and the SiC fiber. Iron particle burning was characterized by individual particle flames shown by the bright spots, and some of these spots were rather large. This means that iron nanoparticles can be ignited and burned only near or within the flame zone. Some particles (most likely large particle aggregates) exploded shortly after ignition, as shown in Fig. 10(2) and Fig. 10(4) at t = 0.117 s and t = 0.372 s, respectively, or formed jets in multiple directions, as shown in Fig. 10(7) and Fig. 10(8) at t = 0.495 s and t = 0.507 s, respectively. The data presented in Fig. 7(d) suggests the occurrence of a strong micro-explosion at $(t/d_0^2) = 2.35$ when (d^2/d_0^2) spiked to 10.42. This process happened quickly and aggressively and has similarities to particle jetting in metalized explosives [39]. This phenomenon is very likely because iron particles are heavy and agglomerate

quickly in liquid. Thus, the smaller droplets and particles ejected from the primary droplet may contain large aggregate structures. A small amount of liquid fuel may be trapped inside the iron particle aggregates. When such aggregates are ejected into the flame zone, quick vaporization of the liquid fuel and potential pressure build-up inside the agglomerate may cause intense breakup of the aggregate and form jetting with significant sparks in multiple directions, as captured in Fig. 10. The increase of oxygen concentration in the liquid may contribute to accelerating the autoxidation process. Referring to Henry's coefficient data from Denisov and Afanasev [40], the coefficient for ethanol is approximately three times greater than that of kerosene, which leads to approximately three times higher oxygen concentration in the fuel at the same partial pressure of oxygen. Micrograph pictures captured by SEM show the effect of the strong intensity of micro-explosion and the distribution of holes on the surface in Fig. S7(c), indicating the full oxidation of the particles as shown in the magnified area in Fig. S7(d).

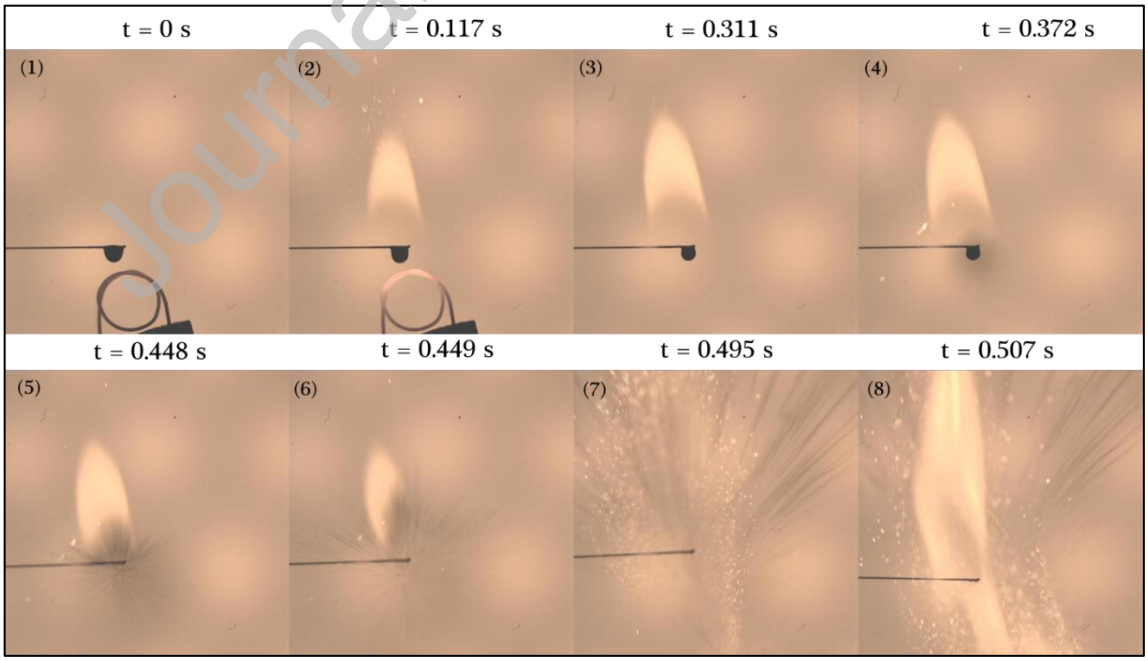

Fig. 10. Time-resolved sequence of images (in seconds, s) of combustion of a single slurry droplet containing 30% Fe (10 μm) in kerosene with 5% ethanol: (1) initial droplet; (2) preheating and ignition; (3) stable combustion; (4) initiation of micro-explosion; (5) high fragmentation and secondary atomization; (6) continued fragmentation and secondary atomization; (7) oxidation of iron particles; (8) jet scattering and near-complete oxidation of iron particles

4.3. Micro-explosion intensity, time of Combustion, and burning rate K (mm²/s)

The volatility differential among fuel constituents in a high-temperature environment leads to the formation of a bubble embryo within the parent droplet. The subsequent growth of this bubble leads to the breakup of the droplet. The disintegration of a multi-component droplet due to this significant volatility differential is known as 'micro-explosion' or secondary atomization. In practice, the occurrence of micro-explosions can potentially enhance fuel atomization in the combustion chamber, which is considered an effective way of promoting efficient combustion in an engine. It is well established from experiments that disruptive burning is primarily dependent on the difference in boiling points of the lower and higher volatile fuel constituents as well as on the appropriate range of relative concentration of alcohol and alkane constituents. As the proportion of ethanol increases in the blends, the probability of micro-explosion increases, while the droplet lifetime decreases. It has been experimentally proven that the likelihood of an abrupt explosion is higher in cases of lower ethanol concentration than in higher concentrations. Another phenomenon is puffing, which is defined as the process during which partial breakup of the parent fuel droplet occurs [41]. At the same time, micro-explosion is the complete breakup of the fuel droplet into small droplets [42,43]. These phenomena often appear together. They originate from the same basic physical processes of nucleation and bubble growth. According to Singh et al., micro-

explosion occurs when the droplet's internal temperature surpasses the homogeneous nucleation temperature of the fuel component, resulting in the formation and growth of a vapor bubble within the fuel droplet [44]. In this process, the occurrence probability of micro-explosions is affected by the droplet temperature and the superheat limit through the nucleation rate of the fuel droplet [45]. The puffing and explosion phenomena can be observed as a rapid spike and dip, respectively, in the evolution of the $(d/d_0)^2$ data for a given droplet Fig. 7(c). Avedisian et al. [43] described two types of micro-explosions: "balloon burst" and "spitting." Fe-40 nm displays the spitting micro-explosion which is with lower intensity, whereas Fe-10 μm exhibits balloon-burst micro-explosions Fig. 7(d). In contrast to these multicomponent fuels, single-component fuels such as kerosene display very little to no micro-explosions Fig. 7(a). The puffing and explosion phenomena can be observed as a rapid spike and dip, respectively, in the evolution of $(d/d_0)^2$ for a given droplet (see Fig. S6(a)) and Equation 2. This information can be used to characterize micro-explosion intensity. The intensity of the micro explosion for the process can then be represented by Equation (2):

$$I = \frac{\left[\left(\frac{d}{d_0}\right)_b^2 - \left(\frac{d}{d_0}\right)_a^2 + \left(\frac{d}{d_0}\right)_b^2 - \left(\frac{d}{d_0}\right)_c^2\right]}{[t_c - t_a]} \qquad (2)$$

where I is the intensity of the frequency of micro-explosion/puffing events (in s^{-1}) occurring in the evolution of the droplet, $\left(\frac{d}{d_0}\right)_a^2$, $\left(\frac{d}{d_0}\right)_b^2$, and $\left(\frac{d}{d_0}\right)_c^2$ are the normalized squared diameters at points a, b, and c, where the puffing and explosion occur from the lowest to the highest, and t is the time.

Multiple puffing/micro-explosion of 30% Fe-40 nm + Kerosene, as shown in Fig. S6(a), is characterized by a local maximum followed by a local minimum in the $(d/d_0)^2$ plot. The puffing process occurs from (a) to (b) and is characterized by a sharp rise in

$(d/d_0)^2$. The explosion occurs from (b) to (c) and is marked by a sharp decrease in $(d/d_0)^2$. For all experiments, the intensity of micro-explosion events in Zone marked and magnified was calculated. The average number of micro-explosion events and the average of the intensity frequencies were then calculated. Refer to supplementary material file Table S2.

A graphical representation of the above-mentioned variables for the Case of 30%Fe-40 nm in kerosene with the addition of 5% ethanol is presented in Fig. S6. The micro-explosions observed in the combustion of Fe-10 µm include only one swelling event (spike) and end with the dissociation of the droplet into fine micro-droplets (i.e., no dips) as illustrated in Fig. S6. Therefore, the intensity *I* is defined as the change in $(d/d_0)^2$ from the time swelling begins (point *a*) to the moment explosion occurs (point *b*), expressed by Equation (3).

$$I = \frac{\left[\left(\frac{d}{d_0}\right)_b^2 - \left(\frac{d}{d_0}\right)_a^2\right]}{[t_b - t_a]} \qquad (3)$$

Based on a minimum of five experiments for each case using Equation (3), the average intensity of micro-explosions was found to be 40.6 sec^{-1} for 30% Fe-40 nm particles + kerosene, 424 sec^{-1} for a multicomponent fuel of 5% ethanol in kerosene, and 1736 sec^{-1} for colloids of 30% Fe-40 nm particles combined with kerosene and 5% ethanol, as determined using Equation (2). This increase of approximately 300% demonstrates the significant effect of adding 5% of ethanol. The total intensity is calculated by summing all peaks, and the results are averaged across samples. Notably, in the case of colloids of 30% Fe-10 µm particles in kerosene with 5% ethanol, the intensity of micro-explosions reached 19707 sec^{-1} as calculated by Equation (3). Fig. S6 illustrates this analysis, where the zoomed area, marked with a red line in Fig. S6, represents the micro-explosion performance. This figure reveals a sharp increase for the case of

colloids of 30% Fe-10 µm particles in kerosene with 5% ethanol from $\left(\frac{d}{d_0}\right)^2_a$ =.988 to $\left(\frac{d}{d_0}\right)^2_b$ =12.2 and within a very short time interval $[t_b - t_a] = .0005\ s$.

The burning rate is quantified as the slope of the curve derived from the analysis of normalized data in accordance with the droplet d²-law of combustion, as outlined in Equation (1). Fig. 11(a) illustrates the burning rates for various fuel formulations, with neat Kerosene serving as the baseline at 0.266 mm²/s. Adding 30% Fe-40 nm particles slightly increased it to 0.285 mm²/sec (7.1% increase), while 30% Fe-10 µm particles reduced it to 0.151 mm²/sec (43.2% decrease) due to incomplete combustion. The addition of 5% Ethanol to Kerosene significantly enhances the burning rate to 1.062 mm²/s, marking a substantial increase of approximately 300%. The mixture of 30% Fe-40 nm with Kerosene and 5% Ethanol achieve a burning rate of 0.309 mm²/s, indicating a moderate increase of about 16%. The burning rate of the 30% Fe-10 µm mixture with kerosene and 5% ethanol cannot be included as it does not follow the d^2-classical combustion law due to its shorter duration and single-event micro-explosion. Instead, the micro-explosion effect is more significant, as explained in Fig. S6.

Combustion time is defined as the duration from the initial appearance to the final extinction of the flame in each experiment. Consequently, the droplet burning time is influenced by the combustion rate and mass loss during puffing and micro-explosion events. The chart in Fig. 11(b) delineates the total combustion time for various fuel formulations, using neat Kerosene as the benchmark with a combustion time of 1.418 seconds. The addition of 30% Fe-40 nm particles reduced this to 1.287 seconds (9.2% decrease), while 30% Fe-10 µm particles shortened it further to 0.6405 seconds (54.9% decrease), due to more incomplete combustion from the larger particles and larger surface tension leading to droplet detachment from the fiber. Introducing 5% ethanol to

kerosene drastically reduces the combustion time to 0.673 second, marking a substantial 52.5% decrease. The blend of 30% Fe-40 nm with kerosene and 5% ethanol exhibits a combustion time of 1.201 second, translating to a 15.3% reduction. Most notably, the formulation with 30% Fe-10 µm combined with kerosene and 5% ethanol demonstrates a dramatic reduction to 0.288 second, an impressive 79.7% decrease. These findings underscore the efficacy of ethanol and iron particle additives in significantly enhancing combustion efficiency, resulting in substantial reductions in combustion time across various fuel formulations.

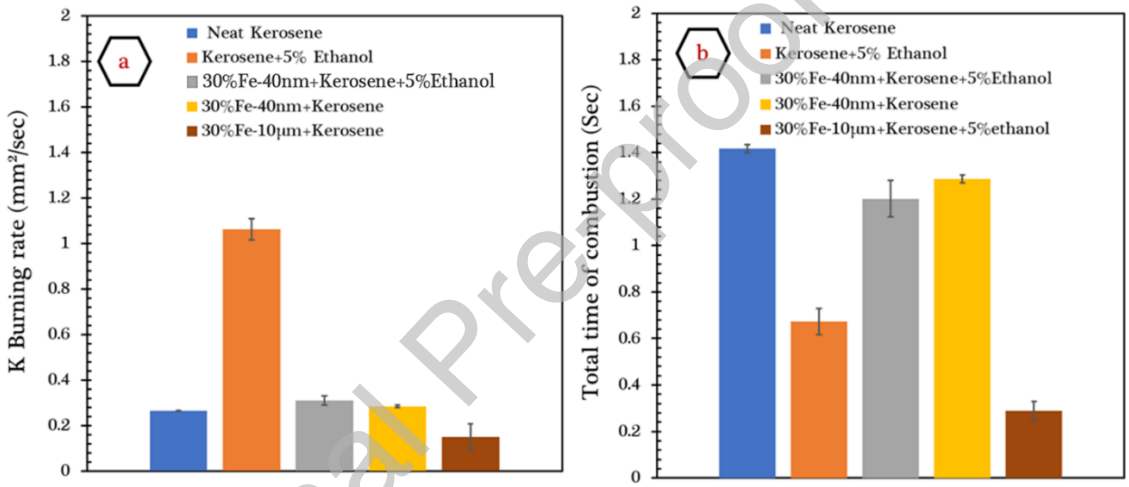

Fig. 11. (a) Droplet burning rate K (mm²/s) and (b) total time of droplet combustion trends of different fuel droplets. Each data point represents the average of five iterations; the error bars indicate the corresponding standard deviation.

Based on the results obtained, the necessity of detecting the maximum internal temperature of slurry iron droplets builds a conceptual framework for understanding the real oxidation temperature, aligning with the TGA-DSC analysis. This explains the mechanisms responsible for the reduction in combustion time and the increase in burning rate. Fig. 12 presents the averaged results of five experiments, with error bars representing the internal temperature of fuel formulations combined with ethanol, which shows significant effects on combustion dynamics. The internal temperature of

neat kerosene was measured at 310°C, consistent with the boiling point of kerosene. After the addition of 5% ethanol, the temperature increased to 323°C, suggesting an enhanced ability to oxidize the iron particles. However, due to the higher thermal conductivity of iron particles compared to the base fuel, heat transfer and diffusion within the droplet are improved. Interestingly, it was observed that the internal temperature dropped from 310 °C to 255 °C in the case of the 30% Fe-40 nm + kerosene + 5% ethanol formulation. In contrast, the temperature rose to 600 °C in the case of 30% Fe-10 µm + kerosene + 5% ethanol, resulting in significant oxidation of the iron particles. This difference can be attributed to the morphological characteristics of the iron particles, which were studied after the post-evaporation process (as described in the experimental methodology). The iron particle agglomerates were collected without triggering ignition and analyzed using a Hitachi TM3030 Tabletop SEM. Fig. 13(a) and Fig. 13(b) show the agglomerates formed with the addition of 5% ethanol for the nano-sized particles. These images reveal that the nanoparticles spread more on the SiC fiber due to ethanol's higher boiling point and lower viscosity compared to kerosene. However, the central iron nanoparticles form a very smooth shell, leading to strong agglomeration that impedes the oxidation process. The rapid formation of the iron oxide shell, coupled with the larger specific surface area of the nanoparticles, results in a less porous structure, and the internal temperature remains at 255°C, insufficient for sustained oxidation. In contrast, the agglomerates of nano-sized iron particles, shown in Fig. 13(c) and Fig. 13(f) for the 30% Fe-40 nm + kerosene formulation, are more spherical and exhibit a weaker tendency to spread on the SiC fiber. This explains the limited increase in the burning rate and total combustion time, as the rapid agglomeration prevents efficient combustion. Ethanol's effect in reducing agglomeration is evident when comparing combustion residues in Fig. S7 and Fig. S3.

Fig. 13(d) and Fig. 13(e) depict the post-evaporation agglomerates of micron-sized iron particles in the 30% Fe-10 µm + kerosene + 5% ethanol case, which are notably porous and less centric compared to the nano-sized case. The porous structure allows ethanol, due to its volatility, to diffuse between the iron particles, forming a gel-like structure around them. This rapid buildup of vapor pressure triggers intense micro-explosions, with ethanol facilitating faster heat transfer to the iron particles. This enhances the local temperature around the particles, helping them to reach their oxidation temperature more rapidly. The heat released by ethanol combustion accelerates heat diffusion to the iron particles, speeding up the oxidation process and resulting in more complete combustion, as evidenced by Fig. S7(c) and Fig. S7(d). This occurs early in the combustion process, reducing the total combustion time. Additionally, these findings provide insight into the sub-droplet detection and jets of oxidized iron particles, explored in Section 4.4.

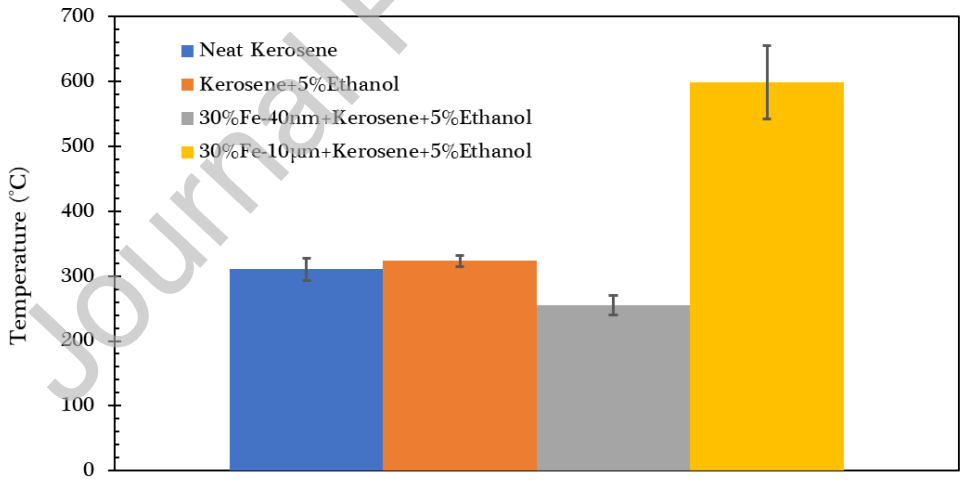

Fig. 12. Droplet maximum internal temperature in (°C) of droplet combustion trends of different fuel droplets, the error bars show the related standard deviation of five iterations

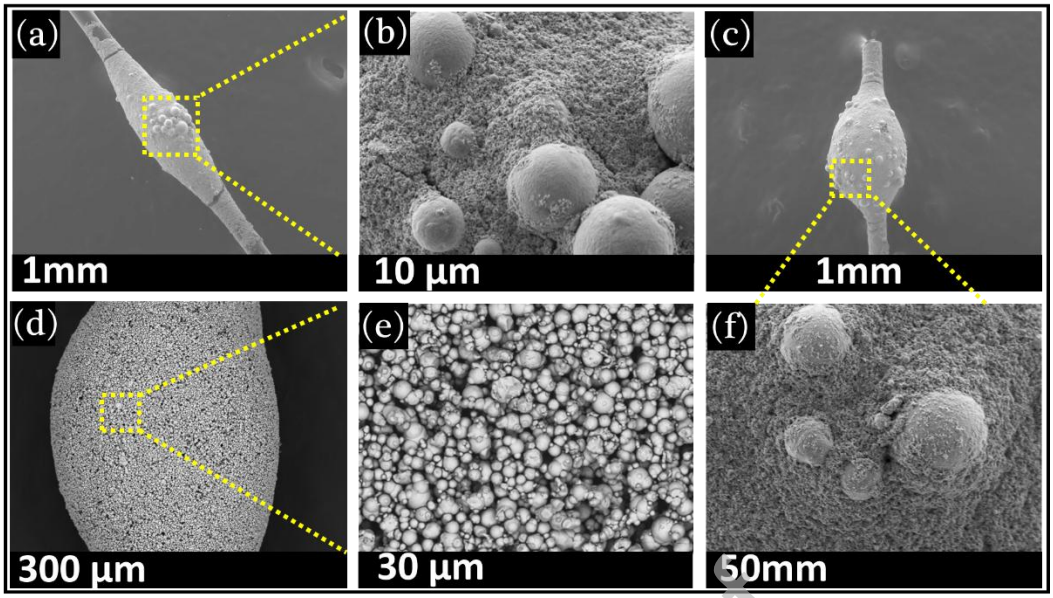

Fig. 13. SEM images of post evaporation leading to particle agglomerates (a), (b) (30% Fe-40 nm + kerosene + 5% ethanol); (d), (e) (30% Fe-10 µm + kerosene + 5% ethanol); (c), (f) (30% Fe-40 nm + kerosene)

4.4. Detection of micro explosion jets and sub droplets

Advanced image processing enabled reliable detection and quantification of sub-droplets and oxidized iron jets during fuel-droplet combustion in Fig. 14. Preprocessing grayscale conversion in Fig. 14(b), Gaussian blur, and sharpening reduced noise and enhanced edges, even under uneven lighting. Adaptive thresholding then binarized images to distinguish particles from background, while morphological closing/opening suppressed residual noise and accentuated small features. Connected-component analysis labeled and measured particles, applying a 5-pixel size threshold to exclude artefacts, which markedly improved counting accuracy and agreed with visual inspection. In experiments with 30 wt% micron iron particles in kerosene + 5% ethanol, high-speed imaging at 2,000 fps across 778 frames in Fig. 14(c) yielded an average of 1,093 sub-droplets/jets per run (range: 863–1,490; n = 3 independent experiments; 7%

error), significantly higher than in control tests. DSC measurements reveal that post-evaporation morphology strongly influences combustion intensity. The Fe-10 μm powder shows a total exothermic heat release of ~37.4 J when coated, while the Fe-40 nm powder releases only ~0.27 J. This two-order-of-magnitude difference correlates with distinct SEM-observed morphologies: porous agglomerates for micron particles and dense aggregates for nanoparticles. Porous agglomerates facilitate deeper oxidant penetration and more complete combustion, resulting in higher heat release and micro-explosion intensity. In contrast, dense aggregates hinder oxygen access and lead to early passivation, reducing energy output. Notably, agglomerates consist of loosely connected particles held by weak forces, while aggregates involve strongly bonded or fused particles that may evolve into compact or spherical forms under thermal conditions [76]. This increase indicates that iron additives intensify micro-explosions, promoting finer droplet breakup and shorter combustion times. SEM of combustion residues corroborated these findings, revealing a distinct morphology consistent with enhanced combustion. Although overlapping particles and variable illumination occasionally caused misidentifications, optimized parameters minimized such errors, yielding high sub-droplet detection fidelity. Full, detailed code is provided in the Appendix E. This technique can help in metallized jet fragmentation detection in metallized composite solid propellants [46–48].

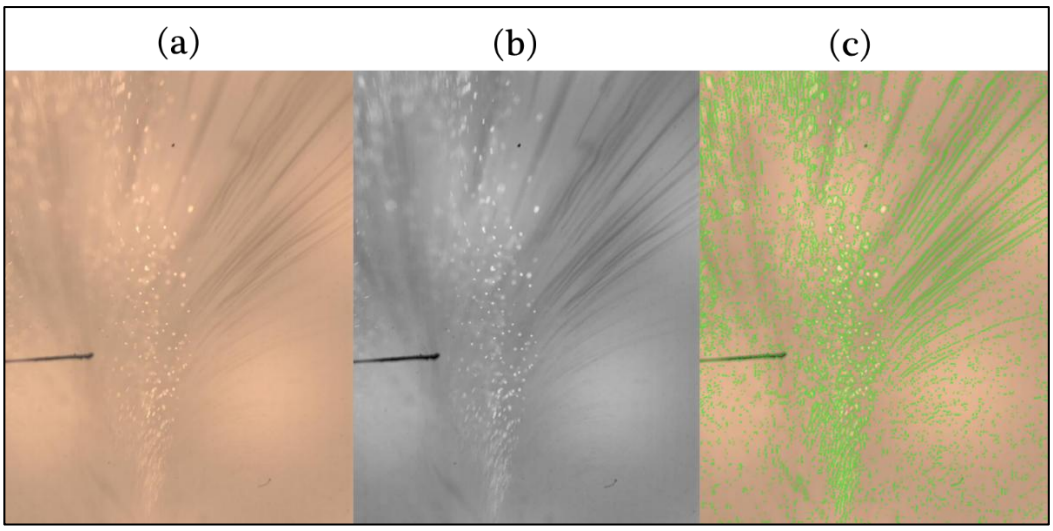

Fig. 14. Image-processing workflow for detecting sub-droplets and jetting oxidized iron particles from a slurry droplet (30 wt% Fe, 10 μm) in kerosene with 5% ethanol: (a) original image; (b) grayscale after preprocessing; (c) final processed/binarized image for particle/jet detection (adaptive thresholding and noise filtering).

Overall, the high-speed imaging, image-processing and SEM results provide a consistent picture: micro-explosions and sub-droplet/jet formation govern the size, morphology and dispersion of the iron-oxide fragments produced during droplet combustion. These combustion residues are not merely by-products, but constitute the feedstock for the subsequent hydrogen reduction and FAST consolidation steps. Their composition and microstructure are therefore expected to influence both the efficiency of reduction and the properties of the consolidated iron. In the next section, the reduction behavior and FAST response of these combustion-derived iron-oxide powders are examined, thereby closing the link between single-droplet combustion and bulk material performance.

4.5. Iron Oxide to Iron: Reduction, Consolidation (FAST), and Vickers Microhardness

Building on the combustion analysis in Sections 4.1–4.4, the subsequent step is to determine whether the solid residues generated by micro-explosive droplet burning can be transformed back into dense metallic iron. Iron-oxide powders collected from the droplet combustion experiments were subjected to hydrogen reduction at 800–900 °C and subsequently consolidated by FAST. Energy-dispersive X-ray spectroscopy (EDS) was performed on selected regions of the hydrogen-reduced powder to quantify the degree of reduction and evaluate compositional uniformity.

Energy-dispersive X-ray spectroscopy (EDS) analysis was performed on sixteen selected regions of the hydrogen-reduced powder (Spectra 32–47, Fig. 15; see Figs. S11–S22 for additional data). The iron (Fe) content in these regions ranged from 69.3 wt % (Spectrum 35, Fig. 15) to 94.1 wt % (Spectrum 46, Fig. S21), with an average of 84.4 wt %. Several spectra (Nos. 39, 43, 44, 46; Figs. S14, S18, S19, S21) exceeded 90 wt % Fe, indicating near-complete reduction, whereas lower-Fe areas (Spectra 34, 35) likely retained oxide or carbonaceous residues. Such incomplete reduction even at 800–900 °C aligns with Bahgat and Khedr's observations of magnetite–hydrogen kinetics: at 900 °C, the $Fe_3O_4 \rightarrow Fe$ conversion slows markedly near 80 % completion because dense Fe layers impede H_2 diffusion [49]. Elemental mapping in Fig. 16 corroborated the EDS findings: Fe was found ubiquitously, while O was concentrated around spherical surface regions (residual oxides) and C appeared in isolated zones (residues); sulfur and silicon (S/Si) were detected only as trace impurities. These maps reveal spatial heterogeneity, with some areas fully metallic and others still partially oxidized, reflecting the local interplay of temperature, gas flow, and particle morphology during reduction [50]. During hydrogen reduction ($Fe_2O_3 + 3H_2 \rightarrow 2Fe + 3H_2O$), the produced water vapor can induce local surface sintering of fine particles or fracturing of larger grains, as illustrated by the yellow rectangle in Fig. 15. Repeated combustion-reduction

cycles would further exacerbate fragmentation, sintering, and clustering (yellow arrows in Fig. 15), degrading particle integrity beyond the classical “shell-expansion” model [51–52]. Therefore, a single reduction cycle is preferable to preserve particle morphology; if finer powder is needed, reprocessing (e.g. via arc atomization) can regenerate fine particles for reuse, enhancing circularity.

In conventional powder-metallurgical processing of iron, near-net-shape components are typically obtained by uniaxial cold pressing of water-atomized or sponge iron powders at several hundred megapascals, followed by furnace sintering in a controlled atmosphere for tens of minutes to hours, so densification is driven purely by external heating and thermally activated diffusion [63–66]. This mature press–sinter route is economical and highly scalable, but its long thermal cycles promote grain growth and leave a residual interconnected porosity that limits mechanical performance; for example, conventionally annealed or sintered high-purity iron generally exhibits Vickers hardness values of only ~30–80 HV, and statistically optimised press–sinter studies on light-metal and ferrous PM systems still report hardness on the order of ~80–120 HV despite careful tuning of compaction pressure, sintering temperature and dwell time [67–69]. By contrast, Field-Assisted Sintering Technology / Spark Plasma Sintering (FAST/SPS) passes a pulsed DC current through a conductive graphite die (and, for conductive powders, the compact itself) under uniaxial pressure, producing intense internal Joule heating at particle contacts; typical heating rates of 10^2–10^3 $°C \cdot min^{-1}$ and minute-scale dwells enable near-theoretical densities at substantially lower bulk temperatures than in conventional furnace sintering, while simultaneously suppressing coarsening, breaking down surface oxides and yielding fine-grained microstructures in metals, ceramics and composites [70-74]. Comparative studies consistently show that FAST/SPS achieves faster densification, higher final density and

smaller grain size than conventional furnace sintering for a wide range of alloy and composite systems, translating into enhanced strength and hardness at similar or lower processing temperatures [75]. Within this context, the present micro-explosion-driven iron-fuel cycle exploits FAST as the terminal consolidation step after hydrogen reduction of combustion-derived iron oxides, achieving ~95 % of theoretical density and a Vickers microhardness of ~165 HV in the recycled iron compact roughly twice the hardness range of annealed or conventionally sintered pure iron while maintaining a fine equiaxed α-Fe grain size of a few micrometres; thus, the FAST stage not only closes the circular iron loop but also upgrades the recovered fuel into a structurally superior powder-metallurgy product that directly links metal-fuel combustion to advanced field-assisted consolidation.

Subsequently, the reduced Fe powder was consolidated in an FCT HP D 25 FAST/SPS furnace. The sintering curve (the complete instantaneous sintering dataset is provided as a CSV file in the Supplementary Material) in Fig. S8 shows rapid densification: the sample heated to 800 °C in ~10 min, with significant shrinkage beginning around 400–450 °C (onset of neck formation and pore closure); a 15-minute hold at 800 °C achieved ~95 % of theoretical density, indicating nearly complete consolidation. The FAST process, with its rapid heating rate, localized Joule heating, and plasma activation, efficiently sinters fine powders while limiting grain growth; the total cycle (~30 min) is therefore well suited for processing recycled or combustion-derived materials. Fig. S9 displays the sintered pellet and a metallographic sample for porosity and grain-structure analysis. SEM/EDS on the polished, un-etched surface in Fig. 17 yielded spectra with 86.0 wt % Fe (Spectrum 9) and 95.4 wt % Fe (Spectrum 10), averaging ~90.7 wt % Fe. Minor oxygen (≤1.7 wt %) and carbon (≤3.0 wt %) likely represent thin native oxides and adventitious carbon, while trace aluminum (<0.1 wt %) originates

from polishing. Backscattered electron imaging revealed a dense α-Fe matrix with sparse dark pores, confirming effective reduction and consolidation. Microscopic characterization before and after chemical etching Fig. 18 highlights the FAST-derived microstructure: in the un-etched sample in Fig. 18(a) and Fig. 18(b), optical and SEM images show closed pores in the submicron-to-micron range, corresponding to trapped reaction by-products and gases from millisecond pulsing [53–54]. After etching in Fig. 18(c) and Fig. 18(d), the microstructure exhibits equiaxed α-Fe grains (~5–10 μm) with pores at triple junctions, reflecting rapid neck growth under the applied current and pressure and yielding a fine, high-density structure with minimal grain coarsening [55–56]. X-ray fluorescence (XRF) analysis in Fig. S10 of the pellet surface and center (four 60 s exposures each) revealed only a single dominant Fe peak at ~6.4 keV [57] and no other elements, indicating 99–100 wt % Fe and excellent compositional uniformity. Overall, hydrogen reduction effectively removes oxygen, and the subsequent FAST sintering under vacuum further eliminates residual oxides while densifying the material. The combined chemical and physical processes yield a dense, nearly pure iron product suitable for powder metallurgy, magnetic applications, and composite metalized propellants.

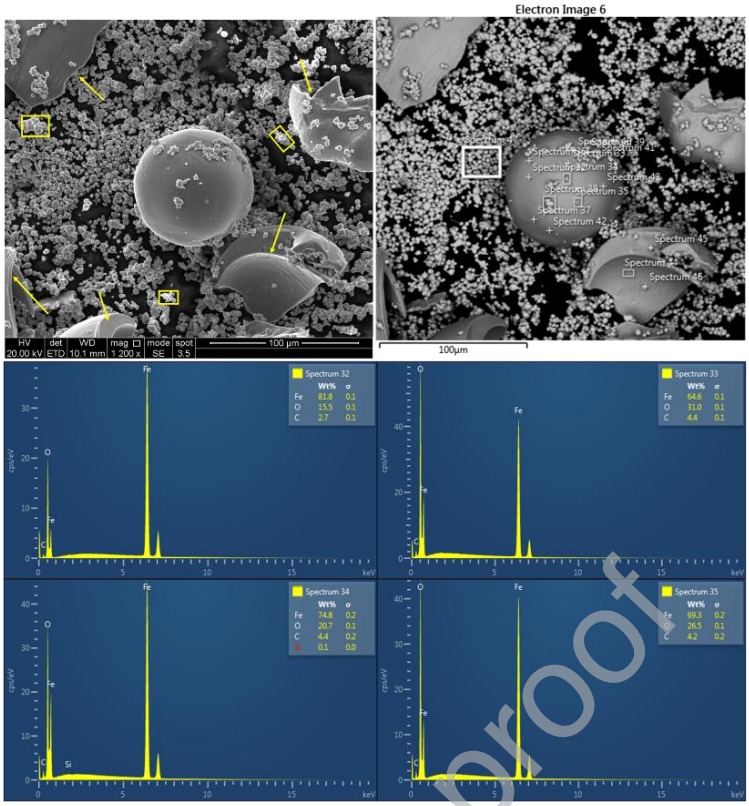

Fig. 15. (EDS) Elemental analysis of reduced iron

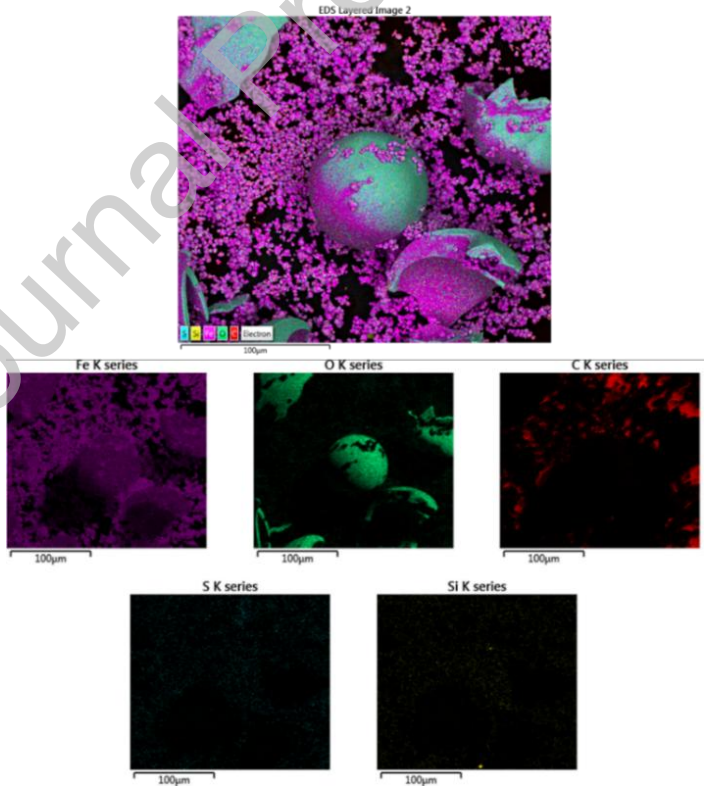

Fig. 16. Mapping of reduced iron particles

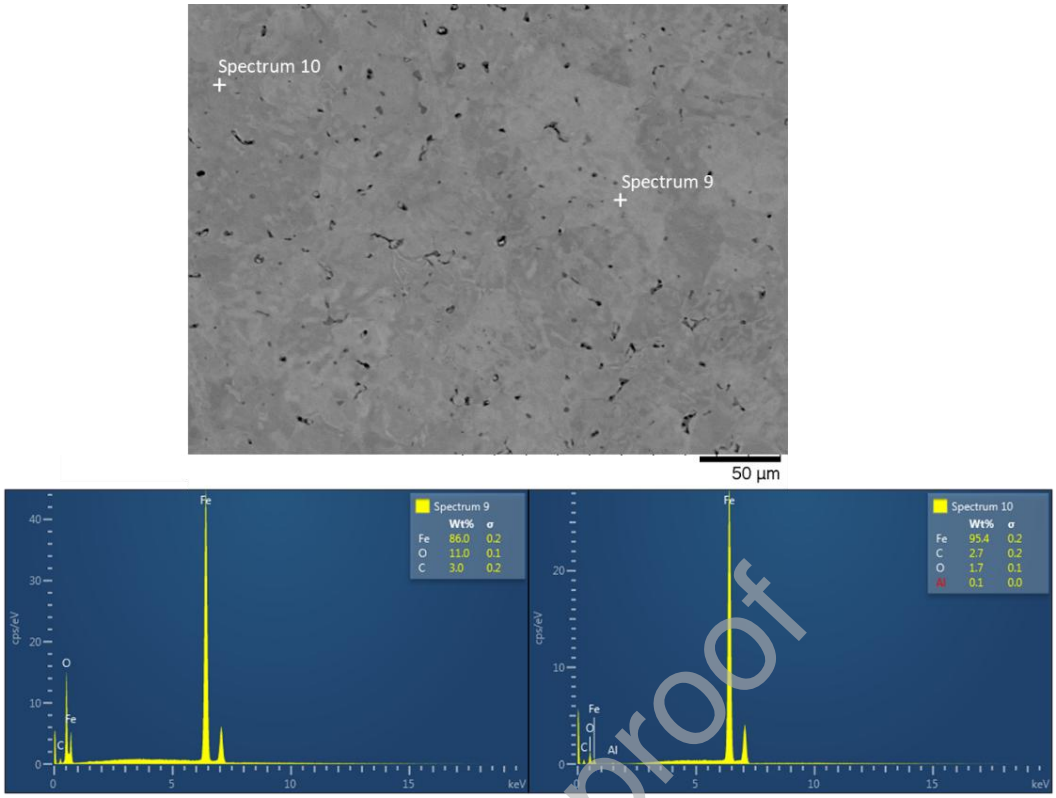

Fig. 17. (SEM/EDS) analysis of reduced iron consolidated via (FAST) before etching

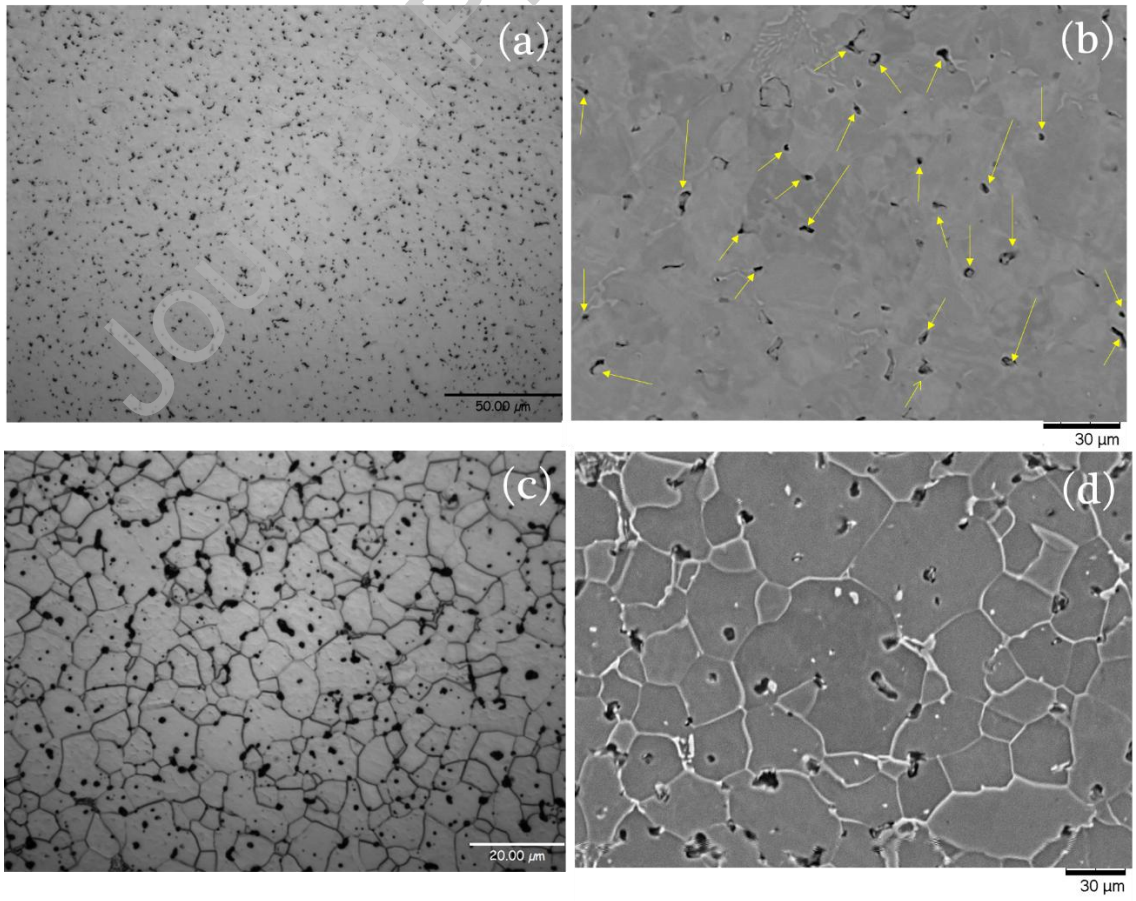

Fig. 18. Microscopic characterization of pore structures before and after chemical etching: (a) optical micrograph of the unetched sample, (b) SEM image of the unetched sample, (c) optical micrograph after etching, and (d) SEM image after etching

In essence, the reduced iron obtained by combustion of micron-sized Fe, followed by hydrogen reduction and FAST sintering, exhibited a Vickers microhardness of 165.44 HV (mean of five indents) as shown in Fig. 19. Compared with 99.9% pure, annealed iron (typically ~70–90 HV), this corresponds to increases of ~+136% vs 70 HV, ~+107% vs 80 HV, and ~+84% vs 90 HV (i.e., ~2.36×, ~2.07×, and ~1.84×, respectively) [58]. Relative to common high-compressibility iron powders (often ≤110 HV), the present value is ~+50% higher [59]; it exceeds many fine-grained ferritic states (~100–125 HV). Although it remains below the hardness achieved by severe plastic deformation or martensitic/pressure-assisted routes (frequently >200 HV and up to ~830 HV for high-pressure martensitic pure Fe), the magnitude of strengthening here is notable given the minimal post-processing [60]. This observation suggests a promising strategy for strengthening consolidated composite materials and may be leveraged in diverse applications, such as shaped-charge components and processing routes for soft magnetic materials.

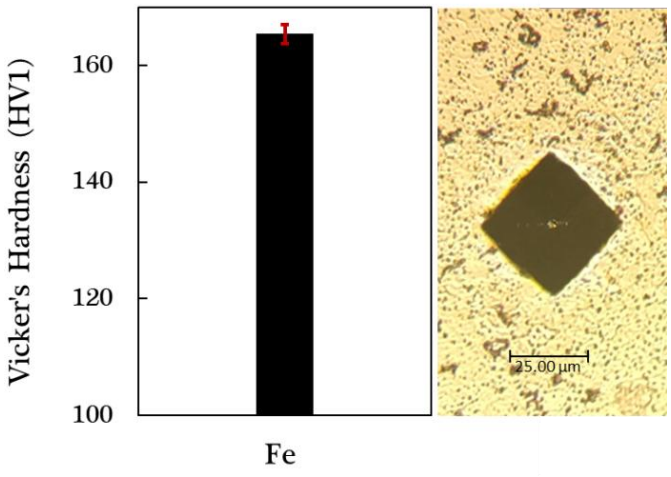

Fig. 19. Vickers hardness of reduced iron after combustion (165.44 HV; mean of five); micrograph shows the identified indentation, and error bars indicate standard deviation.

5. Conclusions

The preservation from oxidation has been demonstrated through the coating of the iron particles with kerosene, and the TGA–DSC represent the kinetics and the role of the micron iron particles as a candidate, which is supported by the proposed micro-explosion mechanism in Fig. 20(a). Within the kerosene + 5 wt% ethanol ferro-slurry, radial heat flux conducted through the high-κ iron matrix pushes the entrained ethanol phase past its homogeneous superheat limit, initiating heterogeneous vapor-embryo formation at metal–liquid interfaces where wettability gradients minimize the nucleation barrier. Because iron's thermal diffusivity is ~30× that of kerosene, latent-heat withdrawal is rapid, and simultaneous gravitational settling of the Fe 10-µm particles forms a porous basal crust that confines the vapor and allows multi-MPa overpressure to accumulate before shell failure. When the Laplace–capillary threshold is breached, the liquid film fragments inertio-capillarily, producing a polydisperse cloud of micron-scale daughter droplets and incandescent iron jets that shorten droplet

lifetime by ≥50% and treble the apparent burning rate. These ejected metal filaments, now stripped of their kerosene coatings, auto-ignite in the oxidizing flame sheet and radiatively preheat neighboring fragments, sustaining recursive puffing cycles until particulate depletion or flame extinction. Then, the iron ash (iron oxides) is subjected to thermal reduction kinetics via hydrogen reduction, which restores the purity of the iron as illustrated in Fig. 20(b). However, the field-assisted sintering technology recovers more than 90% through uniaxial pressure and Joule heating; it increases the electrical conductivity and thermal conductivity as presented in Fig. 20(c) with a very short time to recover this iron content, which leads to closing the cycle of antioxidation followed by successful burning through micro-explosion, followed by hydrogen-reduction kinetics with spark plasma sintering as a dual effect to remove any oxide layer not recovered from the hydrogen reduction, which is leading to conclusion points:

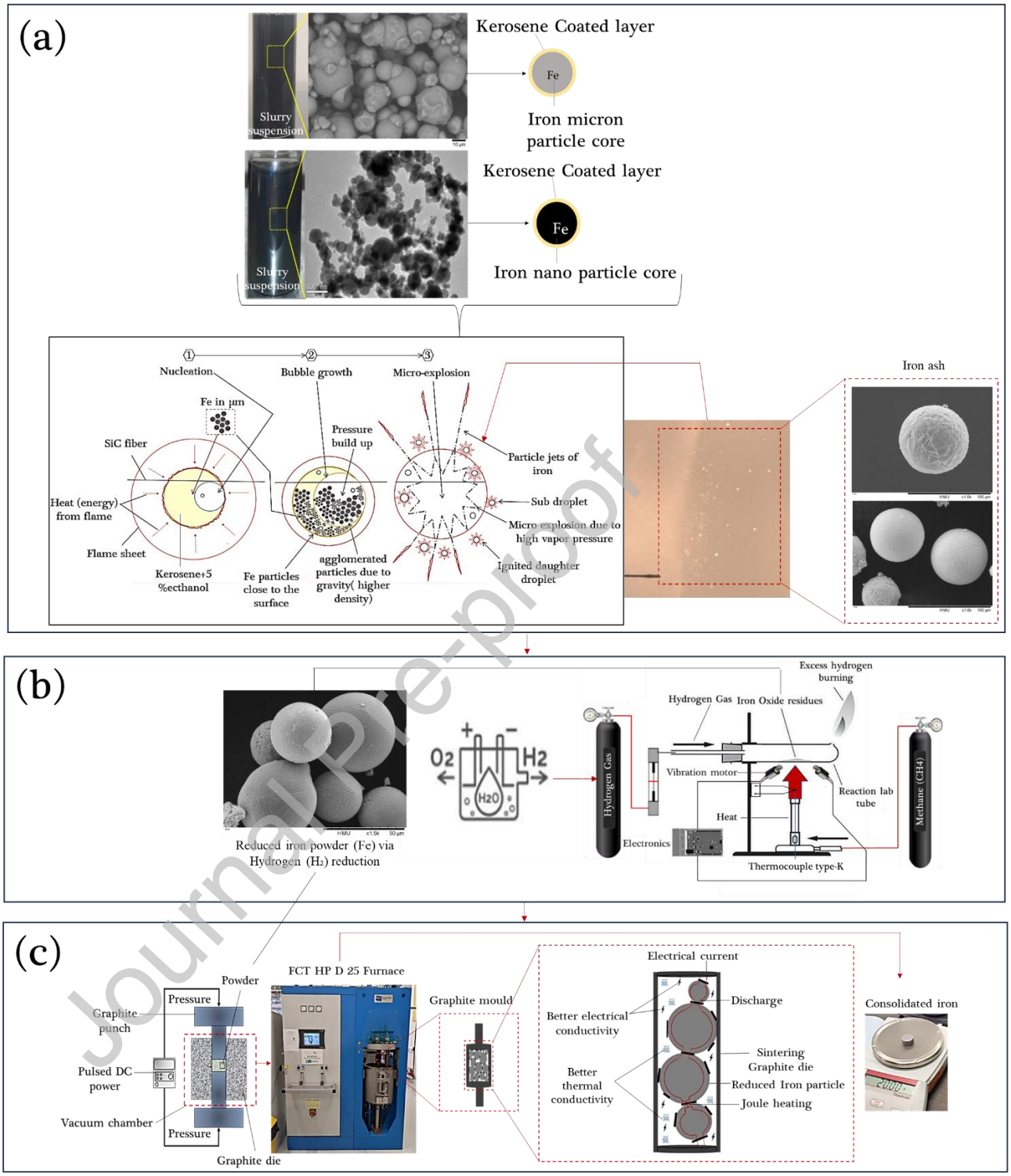

Fig. 20. Closed-loop iron-fuel concept: (a) coated Fe combustion with micro-explosion-assisted oxidation; (b) H_2 reduction of iron oxides to Fe; (c) FAST consolidation of recycled Fe powder.

- Formulating kerosene with 5 wt% ethanol and 30 wt% iron Fe 10-μm enables a dual-purpose micro-explosive fuel and recyclable iron feedstock in a single process chain.

- Ethanol addition markedly enhances combustion: burning rate increased by ~4× and droplet burnout time decreased by ~50% relative to neat kerosene.

- Particle size controls regime: micron-scale Fe produced intense disruptive burning with single, high-magnitude micro-explosions (peak intensity ~1.97×10^4 sec^{-1}; combustion as short as ~0.29 s), whereas nano-Fe exhibited multiple, lower-magnitude events (~1.74×10^3 sec^{-1}) with more gradual burnout.

- The hydrocarbon medium provides an in-situ antioxidation effect, delaying iron oxidation during heating/ignition and supporting non-oxidative interim storage.

- Post-combustion oxides were hydrogen-reduced at 800–900 °C with high yield (~>90% metallic Fe recovered), confirming a practical regeneration route.

- FAST/SPS consolidation of the reduced powder achieved rapid densification (~95% theoretical density) with limited grain coarsening and a fine, equiaxed α-Fe microstructure.

- The consolidated material delivered a Vickers microhardness of 165.44 HV (mean of five indents), exceeding typical 99.9% pure, annealed iron (~70–90 HV) by ~1.8–2.4×, indicating process-induced strengthening

(grain refinement, high dislocation density, and possible dispersion/solution hardening).

- Internal thermometry and SEM/EDS corroborated the distinct oxidation pathways for nano vs. micro iron (dense shell formation versus porous agglomerates), explaining the different combustion intensities and burnout times.

- Image-based diagnostics reliably quantified sub-droplet and jet formation, linking fragmentation statistics to ethanol content and particle size, and validating the micro-explosion mechanism.

- The integrated combustion → oxide capture → H_2 reduction → FAST sequence demonstrates a closed-loop, low-carbon workflow that couples energy release with materials recovery.

The strengthened, consolidated iron is directly relevant for soft-magnetic components and densified metal parts (e.g., liners or inserts), illustrating dual-use potential: energetic performance in combustion and enhanced mechanical utility after regeneration. The full cycle burning iron-laden droplets (combustion), collecting residual iron oxides for hydrogen reduction (regeneration), and consolidating the reduced iron via FAST (reprocessing into billets) enables sustainable recycling of metal fuel and structural materials. Future work should explore alternative liquid fuels, varied O_2 environments, and industrial validation (e.g., furnaces, boilers) to confirm scalability and emission benefits. In addition, the concept is compatible with bio-ethanol, biodiesel, and other oxygenated fuels, where increasing the iron-particle mass concentration can achieve replacement levels above 50–60%. Pilot-scale studies demonstrate promising scalability of iron-based metal fuels: for example, a 1 MW iron-

powder boiler successfully delivered zero-carbon heat to over 500 homes in the Netherlands [80], and laboratory experiments show that iron fuels can complete more than 10 combustion–reduction cycles with stable or improving performance [79]. Safety concerns are manageable through known engineering controls such as wet handling, inserting, and ethanol blending and tests confirm that well-formulated iron powders show low dust cloud propensity and minimal explosion risk under controlled conditions [81]. Life-cycle assessments are encouraging, with closed-loop iron hydrogen systems targeting near-zero CO_2 emissions for industrial heat [78] and achieving round-trip efficiencies in the range of 20–30%, which are competitive with other renewable fuel storage pathways [77].

Declaration of Competing Interest

The authors declare that they have no known competing financial interests or personal relationships that could have appeared to influence the work reported in this paper.

Acknowledgements

This work was supported by the Saudi Arabian Cultural Bureau in London through a PhD scholarship awarded to A.A. The authors gratefully acknowledge the use of the STA thermal analyzer and the support provided by the staff of the Basic Characterization Facility at the University of Sheffield's Royce Discovery Centre. We acknowledge the use of the FAST system and the technical support provided by the workshop team at the Royce Discovery Centre, University of Sheffield.

Author Contributions

- A.A.: Investigation, Conceptualization, Data Curation, Validation, Formal Analysis, Writing – Original Draft, Visualization, Methodology, Invented Experimental Apparatuses, Software, Thermal (TGA-DSC) Analysis, Image Processing,

(SEM/EDS) Preparation and Evaluation, (XRF), Internal Temperature Measurements, Hydrogen Reduction, Field Assisted Sintering Technology (FAST) Consolidation, Metallurgical Sample Preparation, Grain and Porosity Microstructures Evaluation, Vickers microhardness test, Novelty of Micro-explosion Intensity, Novelty of the integrated combustion → oxide capture → H_2 reduction → FAST, Review & Editing

- Y.Z.: Resources, Supervision
- M.G.: Validation, Formal Analysis, Supervision, Writing – Review & Editing
- R.B.: Sub Droplet and Fragmentation detection Algorithms analysis
- I.A.: Review & Editing

References

[1] J. M. Bergthorson, Recyclable metal fuels for clean and compact zero-carbon power, Progress in Energy and Combustion Science 68 (2018) 169-196.

[2] Y. Zhou, J. Liu, D. Liang, W. Shi, W. Yang, and J. Zhou, Effect of particle size and oxygen content on ignition and combustion of aluminum particles, Chinese Journal of Aeronautics 30(6) (2017) 1835-1843.

[3] J. Z. Zhang, Global patterns of phosphorus transformation in relation to latitude, temperature and precipitation, Pedosphere 31(1) (2021) 214-218.

[4] J. M. Bergthorson, Y. Yavor, J. Palecka, W. Georges, M. Soo, J. Vickery, S. Goroshin, D. L. Frost, A. J. Higgins, Metal-water combustion for clean propulsion and power generation, Applied Energy 186 (2017) 13–27.

[5] U. V. Koc, K. R. Liu, Discrete-cosine/sine-transform based motion estimation, Proceedings of the IEEE International Conference on Image Processing (1994) 771–775.

[6] N. Rojas-Valiño, J. Gallego, and A. Santamaría, Effect of an Iron Compound Added to Diesel Fuels in Both Soot Reduction Capacity and Soot Oxidation Reactivity, Energy & Fuels 31(11) (2017) 12455–12465.

[7] J. M. Bergthorson, S. Goroshin, M. J. Soo, P. Julien, J. Palecka, D. L. Frost, and D. J. Jarvis, Direct combustion of recyclable metal fuels for zero-carbon heat and power, Applied Energy 160 (2015) 368-382.

[8] A. Panahi, D. Chang, M. Schiemann, A. Fujinawa, X. Mi, J.M. Bergthorson, Y.A. Levendis, Combustion behavior of single iron particles-part I: an experimental study in a drop-tube furnace under high heating rates and high temperatures, Applications in Energy and Combustion Science 13 (2023) 100097.

[9] J. Sun, P. Liu, M. Wang, Molecular dynamics simulations of melting iron nanoparticles with/without defects using a ReaxFF reactive force field, Scientific Reports 10 (2020) 3408.

[10] J. Wang, Z. Hui, M. Xiao, Research progress of metal fuel motor technology, International Journal of Metallurgy and Metal Physics 5 (2020) 056.

[11] Yetter, R. A., Risha, G. A., & Son, S. F. Metal particle combustion and nanotechnology, Proceedings of the Combustion Institute 32(2) (2009) 1819–1838.

[12] C. E. Bunker and J. J. Karnes, Low-Temperature Stability and High-Temperature Reactivity of Iron-Based Core−Shell Nanoparticles, Journal of the American Chemical Society 126(35) (2004) 10852–10853.

[13] M. Velimirovic, L. Carniato, Q. Simons, G. Schoups, P. Seuntjens, L. Bastiaens, Corrosion rate estimations of microscale zerovalent iron particles via direct hydrogen production measurements, Journal of Hazardous Materials 270 (2014) 18-26.

[14] T. Plachy, E. Kutalkova, M. Sedlacik, A. Vesel, M. Masar, I. Kuritka, Impact of corrosion process of carbonyl iron particles on magnetorheological behavior of their suspensions, Journal of Industrial and Engineering Chemistry 66 (2018) 362-369.

[15] M. Fronczak, O. Łabędź, W. Kaszuwara, Corrosion resistance studies of carbon-encapsulated iron nanoparticles, Journal of Materials Science 53 (2018) 3805-3816.

[16] D. L. Daggett, R. C. Hendricks, R. Walther, and E. Corporan, Alternate fuels for use in commercial aircraft, ISABE Conference 18 (2007) 2007–1196.

[17] C. Sayin, Engine performance and exhaust gas emissions of methanol and ethanol-diesel blends, Fuel 89(11) (2010) 3410–3415.

[18] S. Kumar, J. H. Cho, J. Park, and I. Moon, Advances in diesel-alcohol blends and their effects on the performance and emissions of diesel engines, Renewable and Sustainable Energy Reviews 22(C) (2013) 46–72.

[19] X. Wang, G. Wang, L. Wang, J. Zhang, and J. Yan, Ethanol evaporation characteristics of the blends of fatty acid methyl ester and ethanol, Journal of Shanghai Jiaotong University (Science) 26(2) (2021) 210–217.

[20] J. Han, L. M. T. Somers, R. Cracknell, A. Joedicke, R. Wardle, and V. R. R. Mohan, Experimental investigation of ethanol/diesel dual-fuel combustion in a heavy-duty diesel engine, Fuel 275 (2020) 117867.

[21] Y. Yu, Experimental study on effects of ethanol-diesel fuel blended on spray characteristics under ultra-high injection pressure up to 350 MPa, Energy 186 (2019) 115768.

[22] Lee CC, Tran M-V, Tan BT, Scribano G, Chong CT, A comprehensive review on the effects of additives on fundamental combustion characteristics and pollutant formation of biodiesel and ethanol, Fuel 288 (2021) 119749.

[23] J. Wang, H. Zhang, Q. Zhang, X. Qiao, X. Wang, D. Ju, and C. Sun, Flame spread and combustion characteristics of two adjacent jatropha oil droplets, Fuel 285 (2021) 119077.

[24] Y. Gan, Y. S. Lim, and L. Qiao, Combustion of nanofluid fuels with the addition of boron and iron particles at dilute and dense concentrations, Combustion and Flame 159(4) (2012) 1732-1740.

[25] Aboalhamayie, A., Zhang, Y., Ghamari, M., Iron particle in liquid fuel combustion technology for nonoxidative storage and easy burning, Fuel 380 (2025) 133240.

[26] Pineau, A., Kanari, N., & Gaballah, I, Kinetics of reduction of iron oxides by H_2: Part I: Low temperature reduction of hematite, Thermochimica Acta 447(1) (2006) 89–100.

[27] Hessels, C. J. M., Homan, T. A. M., Deen, N. G., & Tang, Y, Reduction kinetics of combusted iron powder using hydrogen, Powder Technology 407 (2022) 117540.

[28] Cui, G., Wei, X., Olevsky, E. A., German, R. M., & Chen, J, The manufacturing of high porosity iron with an ultra-fine microstructure via free pressureless spark plasma sintering, Materials 9(6) (2016) 485.

[29] Nanostructured & Amorphous Materials, Inc., https://www.nanoamor.com/inc/sdetail/55340 (accessed November 2023).

[30] R. Klimek and T. Wright, Spotlight: Image Analysis and Object Tracking Software, 2004 [Online] Available: [Accessed: July 2019]. https://ntrs.nasa.gov/search.jsp?R=20060011194.

[31] Hicks, M. C., Nayagam, V., Williams, F. A, Methanol droplet extinction in carbon-dioxide-enriched environments in microgravity, Combustion and Flame 157(8) (2010) 1439–1445.

[32] L. Carmignani, Flame Tracker: An image analysis program to measure flame characteristics, SoftwareX 15 (2021) 100791.

[33] Bozkurt, F., Yaganoglu, M., & Günay, F. B, Effective Gaussian blurring process on graphics processing unit with CUDA, International Journal of Machine Learning and Computing, 5(1) (2015) 57.

[34] P. Roy, S. Dutta, N. Dey, G. Dey, S. Chakraborty and R. Ray, Adaptive thresholding: A comparative study, 2014 International Conference on Control, Instrumentation, Communication and Computational Technologies (ICCICCT), Kanyakumari, India, (2014) 1182-1186.

[35] Neethu, P. S., Suguna, R., & Sathish, D, An efficient method for human hand gesture detection and recognition using deep learning convolutional neural networks, Soft Computing 24(20) (2020) 15239-15248.

[36] E. N. Lysenko, A. P. Surzhikov, S. P. Zhuravkov, V. A. Vlasov, A. V. Pustovalov, and N. A. Yavorovsky, The oxidation kinetics study of ultrafine iron powders by thermogravimetric analysis, Journal of Thermal Analysis and Calorimetry 115 (2014) 1447–1452.

[37] Li, J., Li, B., Han, J., Cao, Z., & Wang, J, A comparative study on the reduction mechanism of Fe_2O_3 under different heating methods. JOM 66(8) (2014) 1435–1443.

[38] The Engineering Tool Box, Vapor and saturation pressure for some common liquids [Online]. Available: https://www.engineeringtoolbox.com/vapor-pressure-d_312.html. [Accessed: 30-Jan-2020].

[39] Beloni, E., Hoffmann, V. K., Dreizin, E. L, Combustion of decane-based slurries with metallic fuel additives, Journal of Propulsion and Power 24 (2008) 1403–1411.

[40] E. T. Denisov and I. B. Afanasev, Oxidation and Antioxidants in Organic Chemistry and Biology, CRC Press (2005).

[41] Tsao, K. C., Wang, C. L., Puffing and micro-explosion phenomena of water emulsion fuels, SAE Technical Paper (1986) 860304.

[42] V. M. Ivanov, P. Nefedov, Experimental investigation of the combustion process of natural and emulsified liquid fuels, Published for the National Aeronautics and Space Administration, Washington, DC (1965).

[43] S. Fostiropoulos, G. Strotos, N. Nikolopoulos, and M. Gavaises, A simple model for breakup time prediction of water-heavy fuel oil emulsion droplets, International Journal of Heat and Mass Transfer 164 (2021) 120581.

[44] Singh, G., Esmaeilpour, M., Ratner, A, Investigation of combustion properties and soot deposits of various US crude oils, Energies 12 (2019) 2368.

[45] Mikami, M., Yagi, T., Kojima, N, Occurrence probability of microexplosion in droplet combustion of miscible binary fuels, Proceedings of the Combustion Institute 27 (1998) 1933–1941.

[46] J. C. Thomas, G. D. Lukasik, F. A. Rodriguez, W. D. Kulatilaka, and E. L. Petersen, Combustion of iron particles in solid propellants at elevated pressure, FirePhysChem 4(3) (2024) 252–263.

[47] H. Gao, H. Yu, Y. Tang, X. Yu, W. Zhang, L. T. DeLuca, and R. Shen, Catalytic effects of transition metal oxides on HTPB-based fuel polymer matrices, FirePhysChem 5(3) (2025) 201–208.

[48] B. Prakash, A. Saxena, Y. K. Tyagi, K. Devi, R. K. Tanwar, and A. Kumar, Maltose-based pyrotechnic aerosol forming composites for fire extinguishing application, FirePhysChem 5(2) (2025) 190–200.

[49] Bahgat, M., Khedr, M. H. Reduction kinetics, magnetic behavior and morphological changes during reduction of magnetite single crystal, Materials Science and Engineering: B 138(3) (2007) 251–258.

[50] D. Spreitzer and J. Schenk, Reduction of iron oxides with hydrogen—A review, Steel Research International 90(10) (2019) 1900108.

[51] Wiinikka, H., Vikström, T., Wennebro, J., Toth, P., Sepman, A. Pulverized sponge iron, a zero-carbon and clean substitute for fossil coal in energy applications, Energy & Fuels, 32(9) (2018) 9982–9989.

[52] Sepman, A. S., Malhotra, J. S., Wennebro, J., Wiinikka, H., Iron as recyclable electrofuel: Effect on particle morphology from multiple combustion–regeneration cycles, Combustion and Flame 259 (2024) 113137.

[53] H. G. Mohammed, T. M. B. Albarody, M. Mustapha, N. M. Sultan, and H. K. M. Al-Jothery, Investigate the effect of process parameters of magnetic inductively assisted spark plasma sintering (SPS) of iron oxide (Fe_3O_4) on microstructure behaviour – Part I, Materials Today: Proceedings 42(Part 5) (2021) 2106–2112.

[54] L. Choisez, K. Hemke, Ö. Özgün, C. Pistidda, H. Jeppesen, D. Raabe, Y. Ma, Hydrogen-based direct reduction of combusted iron powder: Deep pre-oxidation, reduction kinetics and microstructural analysis, Acta Materialia 268 (2024) 119752.

[55] A. M. Laptev, M. Bram, D. Garbiec, J. Räthel, A. van der Laan, Y. Beynet, J. Huber, M. Küster, M. Cologna, O. Guillon, Tooling in spark plasma sintering technology: Design, optimization, and application, Advanced Engineering Materials 26(5) (2024) 2301391.

[56] Pepper, J., Blanch, O. L., Thomas, B., Jackson, M, Channelling electric current during the field-assisted sintering technique (FAST) to control microstructural evolution in Ti-6Al-4V, Journal of Materials Science 58 (2023) 14514–14532.

[57] S. R. Nalluri, R. Nagarjuna, D. Patra, R. Ganesan, and G. Balaji, Large scale solid-state synthesis of catalytically active Fe_3O_4@M (M = Au, Ag and Au–Ag alloy) core-shell nanostructures, Scientific Reports 9 (2019) 6603.

[58] M. Tomita, T. Inaguma, H. Sakamoto, K. Ushioda, Development of recrystallization texture in severely cold-rolled pure iron, ISIJ International 56(4) (2016) 693–699.

[59] Y. Ozaki, M. Ueta, and N. Nakamura, Highly compressible iron powder, U.S. Patent US 6,638,335 B2, 28 October 2003.

[60] H. Zhang, Y. Wang, Y. Peng, P. Zhu, J. Liu, Z. Feng, G. Wu, and X. Huang, Unprecedented strength in pure iron via high-pressure induced nanotwinned martensite, Materials Research Letters 7(9) (2019) 354–360.

[61] Tanvir, S., Qiao, L, Effect of addition of energetic nanoparticles on droplet-burning rate of liquid fuels, Journal of Propulsion and Power 31 (2015) 408–415.

[62] Noh, K., Kim, H., Nam, S., Song, S, Study on the combustion characteristics of ethanol nanofuel, Aerospace 10(10) (2023) 878.

[63] D. K. Singh, Powder metallurgy, in: Fundamentals of Manufacturing Engineering, Springer, Singapore (2024) 487–498.

[64] A. B. Nagaram, Net-shape consolidation of water-atomised and gas-atomised steel powder towards full density, Licentiate thesis, Chalmers University of Technology, Gothenburg, Sweden (2022).

[65] M. Q. Kareem, T. Mikó, G. Gergely, and Z. Gácsi, A review on the production of 17-4PH parts using press and sinter technology, Science Progress 106(1) (2023) 368504221146060.

[66] J. Wendel, S. K. Manchili, E. Hryha, and L. Nyborg, Sintering behaviour of compacted water-atomised iron powder: effect of initial state and processing conditions, Powder Metallurgy 63(5) (2020) 338–348.

[67] H. E. Cleaves and J. M. Hiegel, Properties of high-purity iron, Journal of Research of the National Bureau of Standards 28 (1942) 643–667.

[68] AK Steel International (Cleveland-Cliffs). ARMCO® Pure Iron – High Purity Iron, Product Data Bulletin. AK Steel International, Cleveland (2022).

[69] Open University. Appendix I – Table of hardness values. In: Manufacturing (OpenLearn free course). The Open University, Milton Keynes (2025).

[70] O. Guillon, J. Gonzalez-Julian, B. Dargatz, T. Kessel, G. Schierning, J. Räthel, and M. Herrmann, Field-assisted sintering technology/spark plasma sintering: mechanisms, materials, and technology developments, Advanced Engineering Materials 16(7) (2014) 830–849.

[71] R. Orrù, R. Licheri, A. M. Locci, A. Cincotti, and G. Cao, Consolidation/synthesis of materials by electric current activated/assisted sintering, Materials Science and Engineering: R: Reports 63 (4–6) (2009) 127–287.

[72] Z. A. Munir, U. Anselmi-Tamburini, and M. Ohyanagi, The effect of electric field and pressure on the synthesis and consolidation of materials: A review of the spark plasma sintering method, Journal of Materials Science 41 (2006) 763–777.

[73] K. V. Kuskov, M. Abedi, D. O. Moskovskikh, I. Serhiienko, and A. S. Mukasyan, Comparison of conventional and flash spark plasma sintering of Cu–Cr pseudo-alloys: kinetics, structure, properties, Metals 11(1) (2021) 141.

[74] P. Cavaliere (Ed.), Spark Plasma Sintering of Materials: Advances in Processing and Applications, Springer, Cham (2019).

[75] J. Wu, X. Wu, Y. Gao, and Z. Yan, Innovations in electric current-assisted sintering for SOFC: A review of advances in flash sintering and ultrafast high-temperature sintering, Applied Sciences 14(10) (2024) 3953.

[76] D. Vollath, Agglomeration and aggregation of particles. Considerations based on the entropy of mixing using a stochastic approach, FirePhysChem (2025, in press).

[77] P. Debiagi, R. C. Rocha, A. Scholtissek, J. Janicka, and C. Hasse, Iron as a sustainable chemical carrier of renewable energy: Analysis of opportunities and challenges for retrofitting coal-fired power plants, Renewable and Sustainable Energy Reviews 165 (2022) 112579.

[78] J. Neumann, Q. Fradet, A. Scholtissek, F. Dammel, U. Riedel, A. Dreizler, C. Hasse, and P. Stephan, Thermodynamic assessment of an iron-based circular energy economy for carbon-free power supply, Applied Energy 368 (2024) 123476.

[79] N. C. Stevens, W. Prasidha, N. G. Deen, L. Meeuwsen, M. Baigmohammadi, Y. Shoshin, L. P. H. de Goey, and G. Finotello, Cyclic reduction of combusted iron powder: A study on the material properties and conversion reaction in the iron fuel cycle, Powder Technology 441 (2024) 119786.

[80] E. Scherpenhuijsen Rom and A. Kana, Iron powder as a fuel on service vessels, in: Proceedings of the 15th International Marine Design Conference (IMDC 2024), Amsterdam, The Netherlands (2024) 1–16.

[81] NFPA 484, Standard for Combustible Metals, National Fire Protection Association, 2019.

Graphical abstract

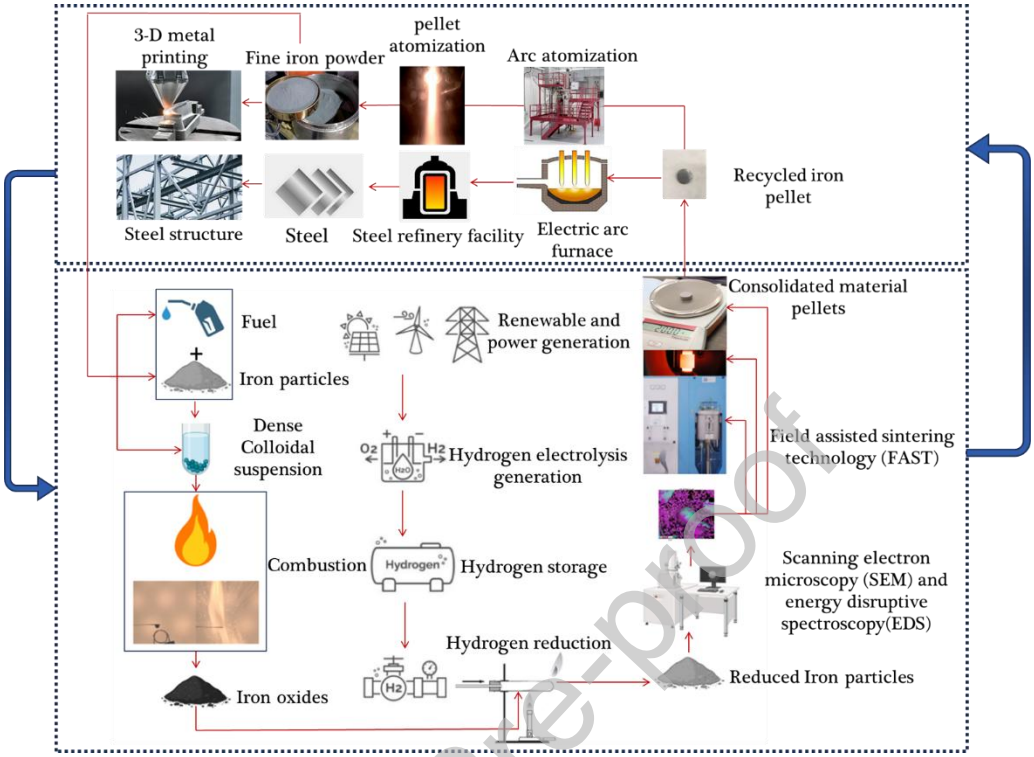

Declaration of Interest Statement

☒ The authors declare that they have no known competing financial interests or personal relationships that could have appeared to influence the work reported in this paper.